



ÉCOLE POLYTECHNIQUE
FÉDÉRALE DE LAUSANNE

MASTER PROJECT

Oxygen Transfer Rate in Orbital Shaken Bioreactors

Author:

Daniel Vito Papa

Supervisor:

Dr. Mohamed Farhat

Assistant:

Matthieu Dreyer

Abstract

As elegant and natural as it is, the "swirling" of a container filled with liquid ensures good mixing and gas exchange. As a matter of fact oenologists have been using it since the dawn of time to aerate the wine before tasting. Swirling (or orbital shaking) is also used in a large variety of biological and chemical applications, as for exemple the culture of mammalian cells. Despite its intensive use the flow generated by orbital shaking is only begining to be understood and a small part of its remarkable richness of patterns is reported as well as a precise knowledge of its Oxygen Transfer Rate. The present study attempt to remedy to this situation by developping an Oxygen Transfer Rate measurement technique to chart its evolution in function of hydrodynamics parameters and wave patterns. Ultimately a novel an undocumented wave pattern is presented.

Acknowledgments

Je tiens tout d'abord à exprimer toute ma gratitude au Dr Mohamed Farhat pour m'avoir ouvert les portes du Laboratoire de Machines Hydrauliques et ainsi donné l'opportunité d'y réaliser mon projet de Master. J'aimerais manifester tout le plaisir que j'ai eu à travailler avec lui, pour ses conseils toujours avisés ainsi que son aide dans les moments plus difficiles et pour les innombrables choses que j'ai eu l'occasion d'apprendre grâce à lui.

Mes remerciements s'adressent également à tous ceux qui directement ou indirectement ont contribué à ce projet, notamment tous les professeurs que j'ai eu la chance de côtoyer. Sans oublier la quantité phénoménale de personnes que j'ai eu l'occasion de rencontrer durant ces belles années d'études et ainsi qu'à tous mes amis, proches ou lointains.

Finalement je voudrais remercier spécialement ma famille : Papa, Maman, Mario, Gui et Matias pour leur soutien continu et indéfectible. Sans vous je ne serais pas la personne que je suis aujourd'hui. Merci du fond du coeur.

Daniel Vito Papa

Lausanne, le 17 janvier 2014

En primer lugar, quiero expresar toda mi gratitud hacia el Dr. Mohamed Farhat por haberme abierto bien grandes las puertas del Laboratorio de M quinas Hidr ulicas, permiti ndome de esta manera tener la posibilidad de realizar mi proyecto de Maestr a. Quisiera tambi n manifestar todo el placer que he tenido al trabajar con  l, y agradecerle nuevamente por su ayuda y apoyo en los momentos m s dif ciles, as  como las innumerables cosas que he podido aprender gracias a su persona.

Mis agradecimientos tambi n van hacia todas las personas que directamente o no contribuyeron con este proyecto, en particular hacia todos los profesores con los cuales he tenido la oportunidad de codearme en estos a os de estudios. No me quiero olvidar de la cantidad fenomenal de gente que conoc  durante estos hermosos a os as  como a todos mis amigos, cercanos como lejanos.

Finalmente quisiera agradecer en especial a mi familia : Pap , Mam , Mario, Guille y Mat as por su apoyo continuo e incondicional. Sin ustedes no ser a la persona que soy hoy en d a. Se los agradezco de coraz n.

Daniel Vito Papa

Lausanne, el 17 de enero 2014

Contents

ACKNOWLEDGMENTS	1
NOMENCLATURE	7
1 INTRODUCTION	9
1.1 HYDRODYNAMICS OF ORBITAL SHAKEN BIOREACTORS : AN OVERVIEW . . .	9
1.2 OXYGEN TRANSFER RATE	13
1.3 MEASUREMENT TECHNIQUES FOR THE OTR, A REVIEW OF THE STATE OF THE ART	14
1.3.1 STEADY STATE METHODS	15
1.3.2 DYNAMIC METHODS	15
1.4 AIM OF THIS STUDY	15
2 EXPERIMENTAL SETUP	17
2.1 EXPERIMENTAL SETUP	17
2.2 OTR DETERMINATION	18
2.3 MEASUREMENT ROUTINE	20
2.4 VALIDATION OF THE MEASUREMENT TECHNIQUE	21
2.4.1 SELF-VALIDATION	21
2.4.2 COMPARISON OF THE PSKM WITH THE GASSING-OUT METHOD	23
3 RESULTS	25
3.1 VERIFICATION OF THE SHAKING FREQUENCY	25
3.2 OTR MEASUREMENTS RESULTS	27
3.3 NON-SYNCHRONOUS WAVE PATTERN AND OTR MEASUREMENTS	30
3.4 DISCUSSION ABOUT THE RESULTS OBTAINED	32
3.4.1 MEASUREMENT TECHNIQUE	32
3.4.2 INFLUENCE OF THE SPECIFIC AREA ON THE OTR	32
3.4.3 SUMMARY	34
4 PECULIAR WAVES	35
4.1 DESCRIPTION	35
4.2 OTR MEASUREMENTS	36
CONCLUSION	38

List of Figures

1.1	EXAMPLES OF ORBITAL MOVEMENT	9
1.2	A : DEFINITION OF THE OPERATING PARAMETERS OF THE ORBITAL SHAKER. B : COORDINATE SYSTEM ASSOCIATED WITH THE ORBITAL SHAKER (FROM [12]).	10
1.3	WAVE PATTERN TRAVELLING INSIDE THE VESSEL FROM RIGHT TO LEFT. A : SINGLE CRESTED WAVE. B : DOUBLE CRESTED WAVE. C : TRIPLE CRESTED WAVE. D : QUADRUPLE CRESTED WAVE. E : WAVE DRYING A PORTION OF THE BOTTOM OF THE VESSEL. F : BREAKING SINGLE CRESTED WAVE. G : WAVE WHOSE PATTERN IS NOT CONSTANT IN A REFERENCE FRAME ATTACHED TO THE VESSEL (FROM [12]).	11
1.4	VISUALIZATION OF THE NATURAL MODES OF THE FREE SURFACE ξ . THE NATURAL FREQUENCIES ω_{mn} OF A LIQUID HEIGHT $\tilde{H}_0 = 0.52$ ARE ALSO GIVEN (FROM [12]).	11
1.5	MEASURED WAVE AMPLITUDES (DEPICTED AS MARKERS) COMPARED TO THE PREDICTION OF THE LINEAR POTENTIAL MODEL (DEPICTED IN SOLID LINES). $\tilde{H}_0 = 0.5$. THE MEASUREMENT IS REALISED FOR FIVE DIFFERENT VALUES OF \tilde{d}_s AND FOR SHAKING FREQUENCIES BELOW THE FIRST NATURAL FREQUENCY ω_{11} (FROM [12]).	12
2.1	EXPERIMENTAL SETUP USED FOR THE MEASUREMENT OF O_2 CONCENTRATION IN THE LIQUID PHASE	18
2.2	EVOLUTION OF THE O_2 CONCENTRATION FOR THREE DIFFERENT VALUES OF $k_L a$. THE FINAL VALUE C_{GL}^* IS THE SAME FOR THE THREE CURVES.	19
2.3	EVOLUTION OF THE O_2 CONCENTRATION FOR THREE DIFFERENT VALUES OF C_{GL}^* . $k_L a$ IS THE SAME FOR THE THREE CURVES.	19
2.4	LINEARIZATION OF O_2 MEASUREMENTS ACCORDING TO EQUATION 2.2 AND THE CORRESPONDING LINEAR REGRESSION AND CONFIDENCE INTERVAL OF 95%.	20
2.5	RESPONSE OF A FIRST-ORDER SYSTEM TO A STEP INCREMENT.	21
2.6	MEASUREMENTS REALIZED FOR THE VERIFICATION OF THE REPEATABILITY OF THE PSKM. THE SQUARE MARKER CORRESPOND TO $\tilde{d}_s = 0.07$, THE TRIANGULAR MARKERS CORRESPOND TO $\tilde{d}_s = 0.1$ AND THE ROUND MARKERS CORRESPOND TO $\tilde{d}_s = 0.13$. $\tilde{H}_0 = 0.5$	22
2.7	EXAMPLE OF TWO LINEAR REGRESSION AND ITS RESPECTIVE CONFIDENCE INTERVAL CORRESPONDING TO A LOW $k_L a$ AND A HIGH $k_L a$	23

2.8	$k_L a$ OBTAINED FROM THE GASSING-OUT METHOD AND FOR THE PSKM METHOD. IN SOLID LINE AND WHITE MARKER IS DEPICTED THE RESULT FOR THE GASSING-OUT METHOD WHEREAS IN DASHED LINE AND GREY MARKER IS DEPICTED THE PSKM METHOD. EACH MARKER CORRESPOND TO A SPECIFIC \tilde{H}_0 . FOR ALL THE MEASUREMENTS $\tilde{d}_s = 0.0656$	24
3.1	UPPER PART : TEN CYCLES OF THE MONITORED SPEED SIGNAL. LOWER PART : INSTANTANEOUS ESTIMATION OF $A(t)$ AND $\omega(t)$ COMPUTED FROM THE SPEED SIGNAL. $\Omega = 90$ RPM, $d_s = 25$ MM.	25
3.2	AVERAGE VALUE OF THE AMPLITUDE $A(t)$ WITH ITS RESPECTIVE STANDARD DEVIATION MAGNIFIED 100 TIMES.	26
3.3	AVERAGE VALUE OF THE FREQUENCY $\omega(t)$ WITH ITS RESPECTIVE STANDARD DEVIATION MAGNIFIED 100 TIMES.	27
3.4	MEASUREMENT OF $k_L a$ IN FUNCTION OF THE ROTATIONAL SPEED Ω NORMALIZED BY THE FIRST NATURAL FREQUENCY ω_{11} . THE VALUES OF \tilde{d}_s ARE $\tilde{d}_s = 0.07$, $\tilde{d}_s = 0.1$ AND $\tilde{d}_s = 0.13$. THE WATER HEIGHT IS $\tilde{H}_0 = 0.5$. IN MARKER ARE DEPICTED THE VALUES OF THE MEASURED $k_L a$ WHILE THE SOLID LINE CORRESPONDS TO THE THEORETICAL VALUE OF THE WATER HEIGHT COMPUTED WITH THE POTENTIAL SOLUTION	28
3.5	EVOLUTION OF THE $k_L a$ DEPICTED AS GREY ROUND MARKERS COMPARED TO THE EVOLUTION OF THE MEASURED AMPLITUDE AT THE CONTAINER WALL δ DEPICTED AS WHITE ROUND MARKERS. IN SOLIDE LINE IS THE LINEAR POTENTIAL PREDICTION OF THE AMPLITUDE AT THE WALL \tilde{A}_δ . $\tilde{H}_0 = 0.5$, $\tilde{d}_s = 0.07$	28
3.6	EVOLUTION OF THE $k_L a$ DEPICTED AS GREY SQUARE MARKERS COMPARED TO THE EVOLUTION OF THE MEASURED AMPLITUDE AT THE CONTAINER WALL δ DEPICTED AS WHITE SQUARE MARKERS. IN SOLIDE LINE IS THE LINEAR POTENTIAL PREDICTION OF THE AMPLITUDE AT THE WALL \tilde{A}_δ . $\tilde{H}_0 = 0.5$, $\tilde{d}_s = 0.13$	29
3.7	EVOLUTION OF THE $k_L a$ DEPICTED AS GREY TRIANGULAR MARKERS COMPARED TO THE EVOLUTION OF THE MEASURED AMPLITUDE AT THE CONTAINER WALL δ DEPICTED AS WHITE TRIANGULAR MARKERS. IN SOLIDE LINE IS THE LINEAR POTENTIAL PREDICTION OF THE AMPLITUDE AT THE WALL \tilde{A}_δ . $\tilde{H}_0 = 0.5$, $\tilde{d}_s = 0.1$	30
3.8	MESUREMENTS OF THE $k_L a$ FOR A NON-SYNCHRONOUS WAVE. THE AVERAGE AND STANDARD DEVIATION ARE REALIZED OVER 5 MEASUREMENTS. $\tilde{d}_s = 0.1$ AND $\tilde{H}_0 = 0.5$	31
3.9	TWO WAVE PATTERNS CORRESPONDING TO THE SAME CONFIGURATION : $\tilde{H}_0 = 0.5$, $\Omega/\omega_{11} = 0.81$, $\tilde{d}_s = 0.1$	31
3.10	GEOMETRICAL PROPERTIES OF A CYLINDRICAL SEGMENT. [6]	32
3.11	EVOLUTION OF THE RATIO a/a_0 AND $k_L a$ IN FUNCTION OF THE WAVE AMPLITUDE $\tilde{\delta}_s$, a_0 BEING THE INITIAL VALUE.	33
4.1	COMPARISON BETWEEN THE PECULIAR WAVE AND THE NON PECULIAR. $\tilde{H}_0 = 0.5$, $\tilde{d}_s = 0.042$, $\Omega/\omega_{11} = 1.75$	35
4.2	EVOLUTION OF THE FREE SURFACE AMPLITUDE OF THE WAVE FOR $\tilde{H}_0 = 0.5$, $\tilde{d}_s = 0.01$ AND VARYING Ω/ω_{11} (FROM [12]).	36

4.3 MEASUREMENT OF THE $k_L a$ FOR HYSTERESIS WAVES DEPICTED BY SQUARE MARKERS PATTERN COMPARED TO THE NORMAL WAVE PATTERN OBTAINED WITH THE SAME CONFIGURATION, DEPICTED BY ROUND MARKERS. $\tilde{H}_0 = 0.5$ 37

Nomenclature

Latin

a	Specific surface area	$[\text{m}^{-1}]$
A	Measured instantaneous shaking speed	$[\text{m s}^{-1}]$
A_δ	Amplitude of the wave at the wall	$[\text{m}]$
$C_{0,\text{L}}^*$	Initial O ₂ concentration in the liquid phase	$[\%]$
$C_{\text{O}_2,\text{GL}}^*$	O ₂ concentration in the gas phase	$[\%]$
$C_{\text{O}_2,\text{L}}$	O ₂ concentration in the liquid phase	$[\%]$
D	Internal diameter of the container	$[\text{m}]$
D_L	Molecular diffusivity of O ₂ in water	$[\text{m}^2 \text{s}^{-1}]$
d_s	Diameter of the shaking circular trajectory, or eccentricity	$[\text{m}]$
$\mathbf{e}_x, \mathbf{e}_y, \mathbf{e}_z$	Basis vectors of cartesian coordinate system	$[-]$
$\mathbf{e}_r, \mathbf{e}_\theta, \mathbf{e}_z$	Basis vectors of cylindrical coordinate system	$[-]$
g	Gravitational acceleration	$[\text{m/s}^2]$
H_0	Liquid elevation in the container at rest	$[\text{m}]$
H	Height of the container	$[\text{m}]$
J_m	Bessel function of the first kind, m^{th} order	$[\text{m}]$
L_{O_2}	O ₂ solubility	$[\text{mg L}^{-1}]$
p	Pressure	$[\text{N/m}^2]$
p_a	Atmospheric pressure	$[\text{N/m}^2]$
$p_{\text{O}_2,\text{G}}$	Partial pressure of O ₂ in the gas phase	$[\text{N/m}^2]$
$p_{\text{O}_2,\text{L}}$	Partial pressure of O ₂ in the liquid phase	$[\text{N/m}^2]$
t_e	Exposure time	$[\text{s}]$
(x, y, z)	Cartesian coordinates of a fluid particle	$[\text{m}]$
(r, θ, z)	Cylindrical coordinates of a fluid particle	$[\text{m}, \text{rad}, \text{m}]$

Greek

δ	Liquid height measured at the wall	$[\text{m}]$
ε_{mn}	n^{th} root of the derivative of the Bessel's function of the first kind, m^{th} order	$[-]$
ϵ_α	Standard deviation	$[\text{h}^{-1}]$
λ	Wavelength	$[\text{m}]$
ξ	Elevation of the free surface predicted by the potential model	$[\text{m}]$
θ	Inclination angle of the elliptic surface of the cylindrical segment	$[\text{rad}]$
ω	Measured instantaneous shaking pulsation	$[\text{rad/s}]$
ω_{mn}	Natural frequency corresponding to the mode (m, n)	$[1/\text{s}]$
Ω	Shaking frequency. Generally notated in revolutions per minutes	$[1/\text{s}]$

Dimensionless

$\tilde{A}_\delta = A_\delta/D$	Measured dimensionless amplitude of the wave at the wall	[-]
$\tilde{A}_\xi = A_\xi/D$	Potentially predicted dimensionless amplitude of the wave at the wall	[-]
$\tilde{d}_s = d_s/D$	Dimensionless shaking diameter	[-]
$\tilde{H}_0 = H_0/D$	Dimensionless unperturbed liquid height	[-]
$\tilde{\delta} = \delta/D$	Measured dimensionless liquid height at the container wall	[-]

Acronims

DAQ	Data Aquisition
OTR	Oxygen Transfer Rate
PSKM	Pressure Step k_La Measurement

Chapter 1

Introduction

1.1 Hydrodynamics of Orbital Shaken Bioreactors : an overview

The orbital shaking is the circular motion of a container maintaining a fixed orientation with respect to an inertial frame of reference at a constant angular velocity. An everyday life example of such a movement is the swirling of a glass of wine, the famous gesture made by oenologist (or simple amateurs) before sniffing the wine. This movement is also used in more technical fields such as biological, chemical and food industry in virtue of its gas exchange and mixing capacity as well as for its affordability and ease to implement.



(a) Wine swirling



(b) Orbital Shaker Bioreactor from Kühner AG

Figure 1.1: Examples of orbital movement

Despite its misleadingly simply and intuitive nature, the orbital shaking movement conceals complicated hydrodynamics phenomenon with an incredibly rich amount of patterns and behaviors. In his PhD thesis Reclari studied the hydrodynamics of orbital shaken bioreactor [12]. The main results of his work will be presented hereafter.

The flow of a liquid contained in an Obital Shaken Bioreactor is a particular case of sloshing. It refers to the movement of fluid inside a moving container. The fluid must have a free surface to constitute a sloshing dynamics problem. An analytical solution for such flow may be provided when some hypothesis are made, namely :

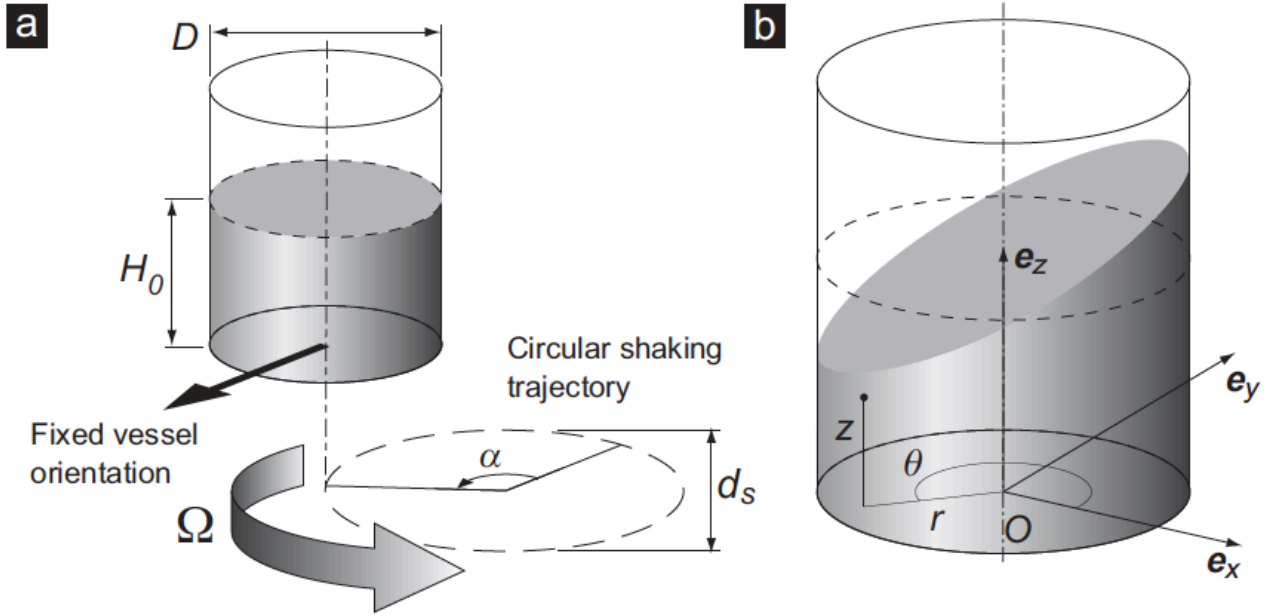


Figure 1.2: **a** : Definition of the operating parameters of the orbital shaker. **b** : Coordinate system associated with the orbital shaker (from [12]).

- The fluid is incompressible
- The fluid is inviscid
- The flow is irrotational

A flow respecting these conditions is called potential flow (since its velocity field can be derived from a potential). The hydrodynamics of the flow depends solely on the four parameters describing the orbital movement and the vessel, namely : the orbit diameter d_s , the diameter of the container D , the liquid height at rest H_0 and the shaking frequency Ω . The motion of the liquid and in particular of its free surface is identified as a wave rotating around the revolution axis the vessel e_z . The potential model predicts that a set of operating parameters leads to one and only one flow and free surface shape. An incredible richness of wave pattern have been identified and some of them are presented in Fig. 1.3.

The linear solution of the potential model predicts the existence of natural modes of the free surface. Each mode possesses its own frequency that can be calculated with Eq. 1.1 :

$$\omega_{mn}^2 = \frac{2g\varepsilon_{mn}}{D} \tanh\left(\frac{2\varepsilon_{mn}H_0}{D}\right) \quad (1.1)$$

where ε_{mn} is the n^{th} root of the derivative of the Bessel's function of the first kind of the m^{th} order. The natural modes are shown on Fig. 1.4. In function of the nature of the excitation of the vessel (lateral acceleration, vertical acceleration, orbital movement etc) the order m is different. *E.g* the orbital shaking movement provokes the first non-axisymmetric mode $m = 1$. Comparatively vertical pulsations are more likely to generate $m = 0$ modes.

These natural modes correspond to the wave patterns observed. The free surface elevation for orbital shaken movement ($m = 1$) can be written in function of (r, θ, t) :

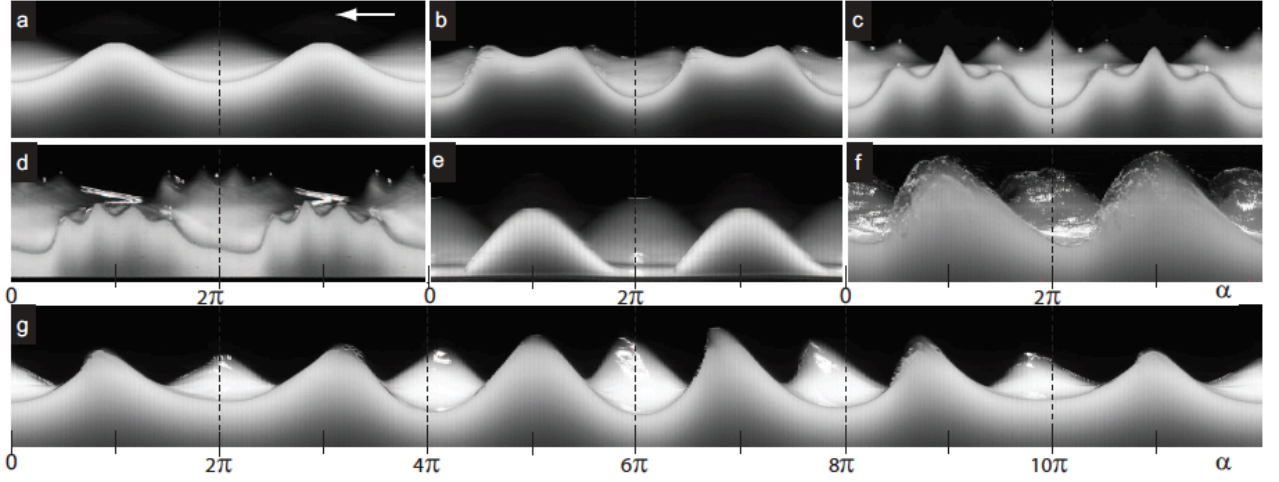


Figure 1.3: Wave pattern travelling inside the vessel from right to left. **a** : single crested wave. **b** : double crested wave. **c** : triple crested wave. **d** : quadruple crested wave. **e** : wave drying a portion of the bottom of the vessel. **f** : breaking single crested wave. **g** : wave whose pattern is not constant in a reference frame attached to the vessel (from [12]).

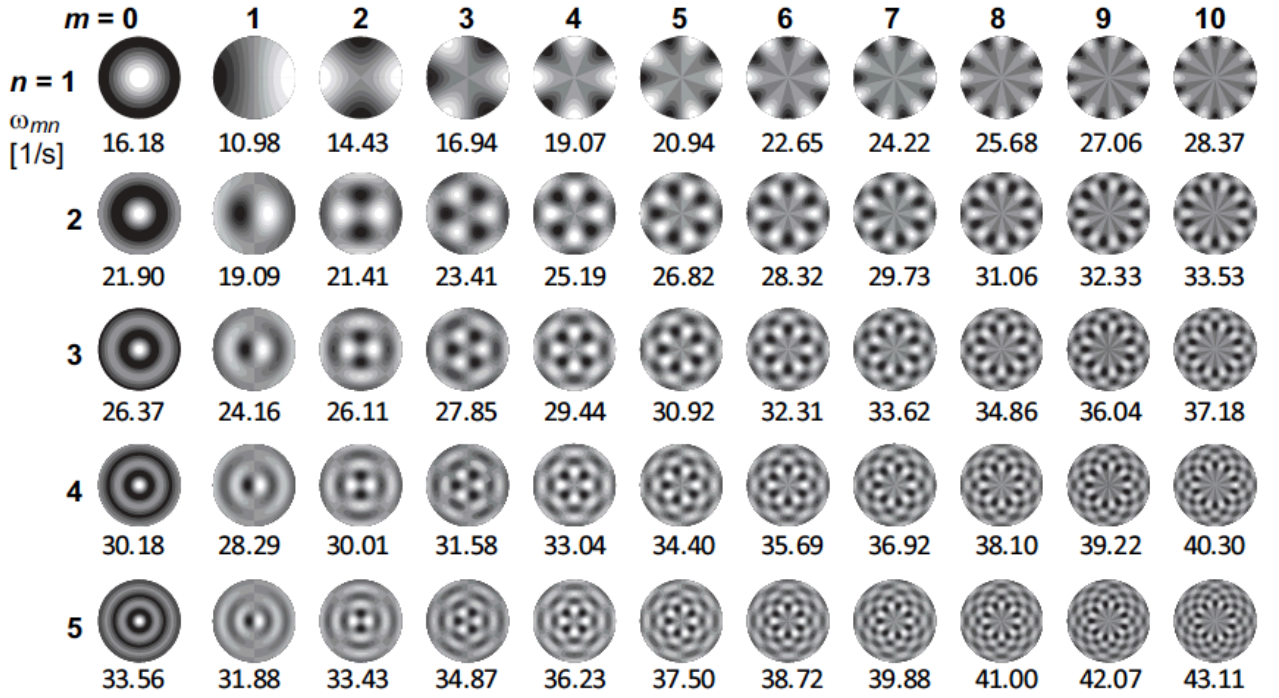


Figure 1.4: Visualization of the natural modes of the free surface ξ . The natural frequencies ω_{mn} of a liquid height $\tilde{H}_0 = 0.52$ are also given (from [12]).

$$\xi(r, \theta, t) = \frac{d_s \Omega^2}{2g} \cos(\Omega t - \theta) \left\{ r + \sum_{n=1}^{\infty} \left[\frac{D}{\varepsilon_{1n}^2 - 1} \frac{\Omega^2}{\omega_{1n}^2 - \Omega^2} \frac{J_1(2\varepsilon_{1n}r/D)}{J_1(\varepsilon_{1n})} \right] \right\} \quad (1.2)$$

where J_1 is the Bessel function of the first kind and first order, r the radial position along the free surface and θ the angular position. The amplitude of the free surface elevation or the crest-to-trough amplitude of the wave at the wall is then written (in adimensional form):

$$\tilde{A}_\xi = \frac{d_s \Omega^2}{g} \cdot \left\{ \frac{1}{2} + \sum_{n=1}^{\infty} \left[\frac{1}{\varepsilon_{1n}^2 - 1} \frac{\Omega^2}{\omega_{1n}^2 - \Omega^2} \right] \right\} \quad (1.3)$$

\tilde{A}_ξ is function of shaking frequency Ω and the eccentricity d_s , *i.e.* the higher Ω and d_s the higher \tilde{A}_ξ . According to the potential model as Ω approaches the first natural frequency ω_{11} the amplitude \tilde{A}_ξ tends to infinite values. Measurement of the amplitude at the wall of the vessel have been realized by Reclari and are found on Fig. 1.5.

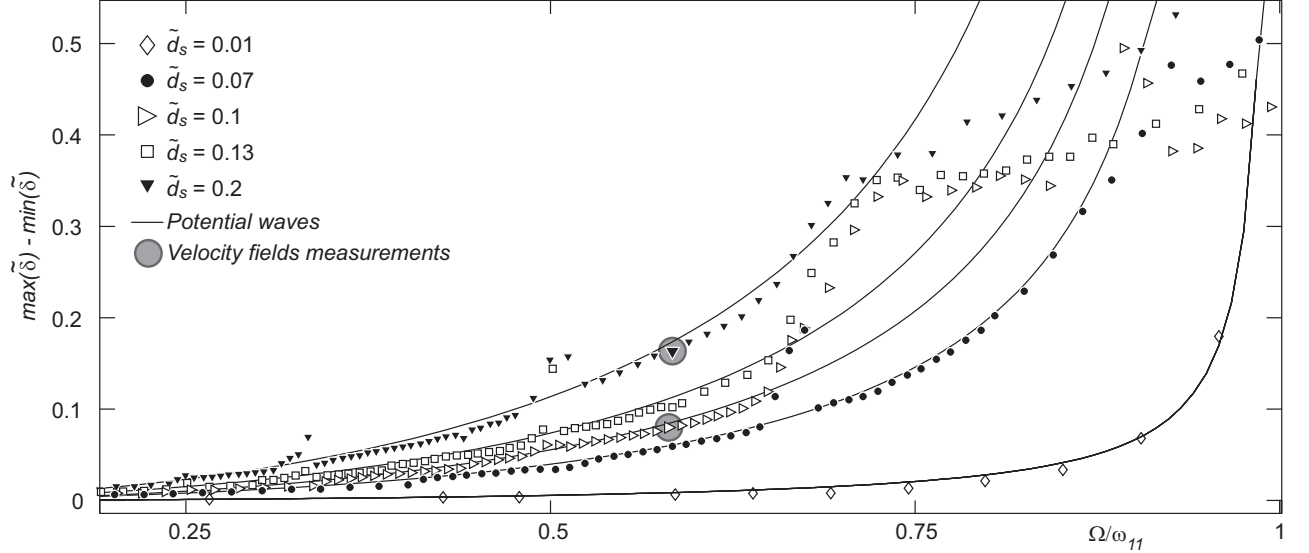


Figure 1.5: Measured wave amplitudes (depicted as markers) compared to the prediction of the linear potential model (depicted in solid lines). $\tilde{H}_0 = 0.5$. The measurement is realised for five different values of \tilde{d}_s and for shaking frequencies below the first natural frequency ω_{11} (from [12]).

As shown on Fig. 1.5 the potential model predicts with remarkable accuracy the amplitude of the wave up to a certain height from which the wave starts to break. The wave breaking phenomenon has been deeply studied in the literature and for gravity wave a limiting steepness exists: $H/\lambda = 0.1412$ where H is the height (crest-to-trough) and λ the wavelength $\lambda = \pi D$. This result has been adapted to the case of the orbital shaken wave pattern :

$$\max(\tilde{\delta}) - \min(\tilde{\delta}) \approx 0.443 \quad (1.4)$$

where $\tilde{\delta} = \delta/D$ is the measured dimensionless liquid height at the wall. Similarly, the other adimensional values are defined as $\tilde{H}_0 = H_0/D$, $\tilde{d}_s = d/D$ (see nomenclature). When the breaking occurs the potential model loses its validity since vorticity and viscous effects are no longer negligible.

One has to note that there are regions where the measured amplitude is higher than the prediction, namely at $\Omega/\omega_{11} = 0.5$ or 0.33 . These regions also correspond to the occurrence of multiple crested waves (see Fig. 1.3b,c,d). These multiple crested waves are not predicted by the linear solution of the potential model but by the non-linear solution. It predicts the existence of sub-harmonic response of the dominant modes namely the mode (1,1), the mode (2,1) and the mode (1,2). Like the mode ω_{11} the sub-harmonics can be also excited. They

are defined as ω_{mn}/p where $p = 1, 2, 3, \dots$ is a positive integer p that also corresponds to the number of crests of the wave. It happens that $\Omega/\omega_{11} = 0.65$ corresponds to the sub-harmonic $\omega_{21}/2$ and it is the reason why there is a peak of amplitude around this frequency (see Fig. 1.5). $\Omega/\omega_{11} = 0.5$ and $\Omega/\omega_{11} = 0.33$ correspond to the sub-harmonics $\omega_{11}/2$ and $\omega_{11}/3$ ($p = 2, 3$ respectively). After the appearance of the sub-harmonic the flow recovers its potential behavior and the wave pattern becomes single crested again. However when $\Omega/\omega_{11} > 0.65$ and $\tilde{d}_s > 0.07$ this is not the case. For those eccentricities the amplitude reached by the wave at resonance with the sub-harmonic is high enough to meet the breaking condition. The flow is then irreversibly changed and does not return to the potential regime.

A final mention has to be made for non-synchronous waves presented in Fig. 1.3g. Almost all waves have in common the periodicity with respect to the shaking frequency. It means that they are motionless in a frame of reference rotating around the container revolution axis at the shaking frequency. However some waves do not respect this condition, *i.e.* they rotate at an angular frequency different from the shaking one. It has to be noted that these are not unsteady waves since they are also periodic, but their periodicity is different from the shaking frequency. The reason of the occurrence of the non-synchronous wave is not known since it has been predicted neither by the linear solution nor by the non-linear. However explanations on their origin exist:

- When the wave arrives at the breaking inception its amplitude decreases due to a loss of energy dissipated by the breaker. It then take some time to the wave which is now in a non breaking configuration to reach its breaking inception amplitude again. The phenomenon is then repeated indefinitely.
- When $\tilde{d}_s < \tilde{d}_{s,\omega_{21}/2} = 0.0971 \cong 0.1$ the wave breaks as single crested and when $\tilde{d}_s > \tilde{d}_{s,\omega_{21}/2}$ the wave breaks as multiple crested. If $\tilde{d}_s \cong \tilde{d}_{s,\omega_{21}/2}$ the flow is found at the boundary. In addition if $\Omega/\omega_{11} > 0.65$ the wave is just at the breaking inception and thus "hesitates" between the two states, breaking or not-breaking.

1.2 Oxygen Transfer Rate

When using bioreactors to cultivate mamalian cells a particular care to O_2 availability in the liquid phase has to be taken since aerobic processes take place in it [17],[4],[14]. These processes can consume the dissolved O_2 at high rate until reaching an desoxygenation of the liquid phase wich is particularly undesired. The equation governing the O_2 transfer also called Oxygen Transfer Rate (OTR) in bioreactors is:

$$OTR = \frac{dC_{O_2,L}}{dt} = k_L a (C_{O_2,GL}^* - C_{O_2,L}) \quad (1.5)$$

where k_L [m/s^{-1}] is the mass transfer coefficient of O_2 in water, a is the specific surface area [m^{-1}], $C_{O_2,GL}^*$ is the O_2 concentration in the liquid phase at the gas-liquid interface [mg/L], $C_{O_2,L}$ is the O_2 concentration in the liquid phase [mg/L] or [%]. The gas-liquid interface is the boundary layer in the liquid phase where the mass transfer take place. *I.e.* its concentration in O_2 is at equilibrium with the gas phase but not with the liquid phase (outside the boundary layer). In other terms it has the same O_2 concentration than the gas phase. The unit [%] corresponds to the percentage of dissolved oxygen in water in comparison to oxygen saturated

water (which possesses 100% dissolved oxygen). Equation 1.5 can be written in terms of the partial pressure of O₂ in the liquid and gas phase:

$$\text{OTR} = \frac{dC_{\text{O}_2,\text{L}}}{dt} = k_L a L_{\text{O}_2} (p_{\text{O}_2,\text{G}} - p_{\text{O}_2,\text{L}}) \quad (1.6)$$

where L_{O_2} is the oxygen solubility [mg L⁻¹]. It clearly appears that the driving force of the OTR is the concentration difference $C_{\text{O}_2,\text{GL}}^* - C_{\text{O}_2,\text{L}}$ or equivalently the pressure difference $p_{\text{O}_2,\text{G}} - p_{\text{O}_2,\text{L}}$. Equations 1.5 and 1.6 are first order differential equation, this means that the solution of these equation are on the form $C(t) = A \exp(-kt) + B$ where k is a time constant. In the precise case of oxygen transfer the time constant can be indentified as $k_L a$. It is then obvious why the $k_L a$ is the fundamental factor in the determination and prediction of the OTR in bio-processes.

In mass transfer theory, $k_L a$ [s⁻¹] is called oxygen transfer coefficient. k_L is described by Higbie's penetration theory [3], [7],[10]:

$$k_L = 2 \sqrt{\frac{D_L}{\pi t_e}} \quad (1.7)$$

where D_L [m² s⁻¹] is the molecular diffusivity, t_e is the exposure time [s]. The diffusivity of the gas in the liquid depends on the gas and liquid involved and cannot be change. However at high agitation speed of the bioreactor this difusivity can be enhanced [13]. Numerous studies in litterature have shown a direct link between the increase of k_L and the increase of turbulence of the free surface, as for exemples [9], [11]. More precisely microscale wave breaking occurring at the free surface is to account for the increase in the k_L [2], [1], [18]. This is not particularly surprising since more turbelence generally enhances the exchanges phenomena, either mass transport, gas exchange or momentum transport.

The specific surface area a is defined by the ratio of the gas-liquid interface area S over the liquid volume V : $a = S/V$. This area is important since it is through it than the gas transfer between the two phases takes place. Increasing the area while keeping the liquid volume constant (achieved through agitation of the liquid bulk) is going to increase a hence the overall oxygen transfer coefficient.

More generally $k_L a$ can be viewed as the "*speed*" of the OTR.

1.3 Measurement techniques for the OTR, a review of the state of the art

Numerous methods for the measurement of the gas transfer velocity exist and can be found in the litterature [14], [4]. There are two main families of measurement techniques, the steady state methods and the dynamic methods. The steady-state methods compute the $k_L a$ from a mass balance of the system. On the other hand the dynamic methods are based on computing the $k_L a$ from the variation of O₂.

1.3.1 Steady State Methods

Sulfite Oxidation Method The sulfate oxidation method is based on the oxydation of sodium sulfite to sulfate by oxygen by the following reaction :



The kinetics of the reation depends on O_2 availability in the liquid phase. This reaction have been studied by many authors and its kinetics is known [14]. The reaction progress can be measured by titrating or electrochemical means and thus allowing to determine the concentration of O_2 in the liquid phase. The k_La is then computed by a mass balance of O_2 stating that the O_2 uptake rate by the reaction and the OTR from the gas phase are at equilibrium

1.3.2 Dynamic Methods

Gassing-out Method The basic principle underlying the gassing-out method is the monitoring of dissolved oxygen concentration after a complete deoxygenation of the given liquid. The monitoring of O_2 should be realized with a fast response non invasive oxygen probe (optical probes are a great compromise). The k_La is then computed through the O_2 evolution in time.

Randomly Pulsed Signal This method is based on the gassing-out method but instead of a complete deoxygenation of the given liquid, the air supply and nitrogen supply are randomly toggle from one to the other. The k_La is then computed numerically. This method have been proposed in [5]

Dynamic Pressure Methods Dynamic pressure method are generally based on the variation of O_2 in the liquid phase achieved through changes in the partial pressure of O_2 in the gas phase. The measurement technique presented in this study is a particular case of Dynamic Pressure Method using a pressure step increment. More details about are found in Section 2.2.

Frequency Response Technique This method is based on a sinusoidal variation of the partial pressure of O_2 in the gas phase [16]. The k_La is then computed either using phase shift information or amplitude modulation.

1.4 Aim of this Study

Despite its wide use in biotechnology the flow generated by the orbital movement is far from being understood. The work of Reclari [12] has brought light to the subject with the discovery of the natural modes of the flow and the remarkable richness of patterns it possesses. However no new information about the OTR has been furnished. Considered its importance in cellular culture and biotechnology in general clarification about its evolution had to be brought.

The aim of this study will be to set and verify an experimental setup capable of measuring the OTR by a dynamic pressure method. This pressure method is based on a step increment of the

O₂ pressure in the gas phase, hence its denomination Pressure Step $k_L a$ Measurement (PSKM) method. The OTR is then going to be monitored in function of the hydrodynamic parameters of the flow. Finally the results obtained are going to be presented.

Chapter 2

Experimental Setup

2.1 Experimental setup

The experimental setup used in this study is presented in Fig. 2.1. The main components are:

- The cylindrical container : inner diameter $D = 190\text{mm}$ and height $H = 220\text{ mm}$.
- The orbital shaker (Khüner AG ES-X lab shaker) with eccentricity d_s varying from 0 to 50 mm and rotational speed Ω varying from 20 to 400 rpm.
- The pressure controller (Festo) with pressure varying from 0 to 2 bar with an internal manometer for pressure monitoring
- The optical dissolved oxygen probe (Fibox 3 from Presens, Germany) along with its corresponding thermometer

The cylindrical container has fixed dimensions and the only parameter that can be changed is the water height H_0 . It is however limited by the height of the container. On top of the container is located a lid containing three holes: one for the pressure inlet, one for the aeration (pressure outlet) and one for a valve. This valve limits the pressure inside the container at 1.424 bar.

On the bottom external wall of the container are attached the dissolved O_2 sensor and the temperature sensor. The optical sensor consists of an optic fiber placed in front of an oxygen sensitive fluorescent spot which has to be in the media where the measurement takes place. In this case the spot is placed in the internal wall of the container and is in contact of the water. The O_2 sensor is based on the Stern-Volmer effect. The sensor emits a time varying light signal through the optic fiber that excites the spot. More detail of this technique is found in the literature [15]. The O_2 and temperature signal are acquired by the Fibox 3 and can be read either by the Fibox 3 software or through the analogical signals obtained.

The pressure is control by a Festo VPPM pressure regulator. The regulator is connected to a pressurized air supply. The device can regulate pressure from 0 to 2 bar if the pressure of the air supplied is at least 4 bar. The pressure is controlled through electrical signal generated externally. The response time of the regulator is better than 0.5 s with a 5 l gas volume. For a container filled with $H_0 = 95\text{ mm}$ of water the corresponding air volume is 3.6 l. The regulator

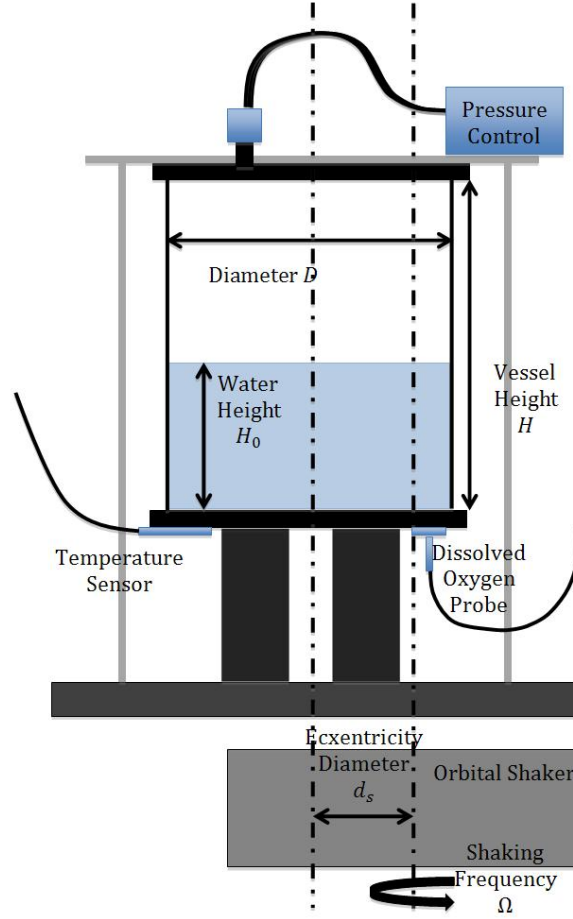


Figure 2.1: Experimental setup used for the measurement of O_2 concentration in the liquid phase

comes with an integrated pressure sensor (accuracy announced is 1%) used to monitor the pressure inside the container through an analogical signal.

The speed and eccentricity are controlled by a Khüner AG orbital shaker. The speed can be set in the range 20 - 400 rpm by step of 1 rpm and the eccentricity in the range 0 - 50 mm by steps of 0.1 mm. Originally the shaker could only provide three predefined eccentricities (12.5, 25 and 50 mm) but the system has been modified to allow continuous variations of d_s [12].

2.2 OTR Determination

The dynamics of O_2 transfer is directed by Eq. 1.5 or Eq. 1.6. As mentioned before they are first order ordinary differential equations whose general solution is of the form $C(t) = Ae^{-kt} + B$ where $k = k_L a$. A and B are identified by the initial and final conditions. At the beginning $C(t = 0) = C_{0,L}$ where $C_{0,L}$ is the initial O_2 concentration in the liquid phase (for simplicity the subscript O_2 is not mentioned since O_2 is the only gas of interest for this study). Similarly $C(t \rightarrow \infty) = C_{GL}^*$ where $C_{GL}^* = L_{O_2} p_G$ is the concentration of O_2 in the liquid phase at the gas-liquid interface or equivalently the pressure of O_2 in the gas phase. The variation of the concentration in time is then written:

$$C(t) = C_{\text{GL}}^* + (C_{0,\text{L}} - C_{\text{GL}}^*)e^{-k_L a \cdot t} \quad (2.1)$$

From this equation the evolution in time of C can be computed and it appears that it depends greatly on the $k_L a$. As a matter of fact the time to reach the asymptotic value is directly related to its value. Some results are shown on Fig. 2.2.

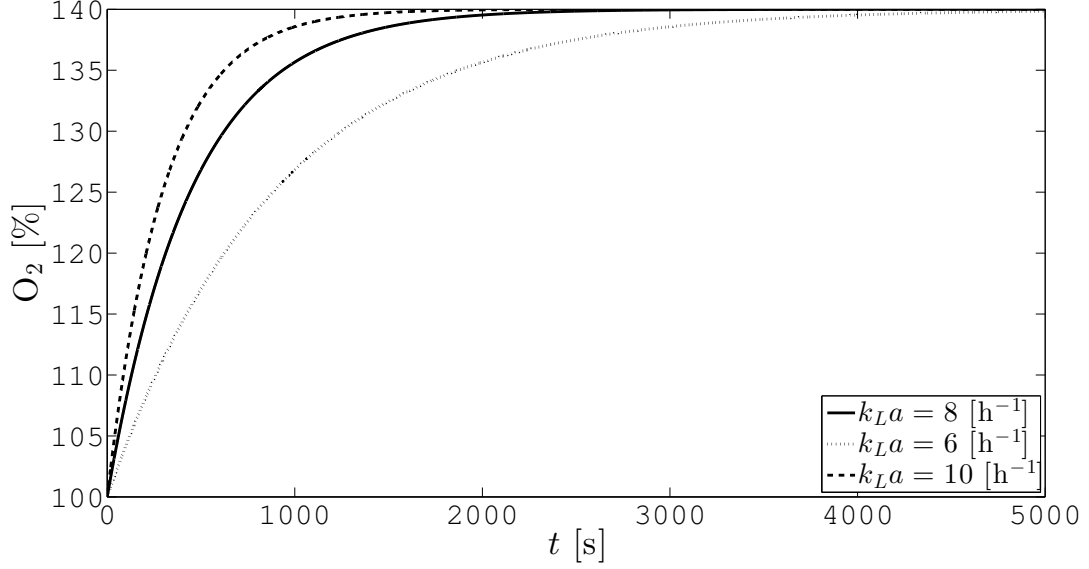


Figure 2.2: Evolution of the O_2 concentration for three different values of $k_L a$. The final value C_{GL}^* is the same for the three curves.

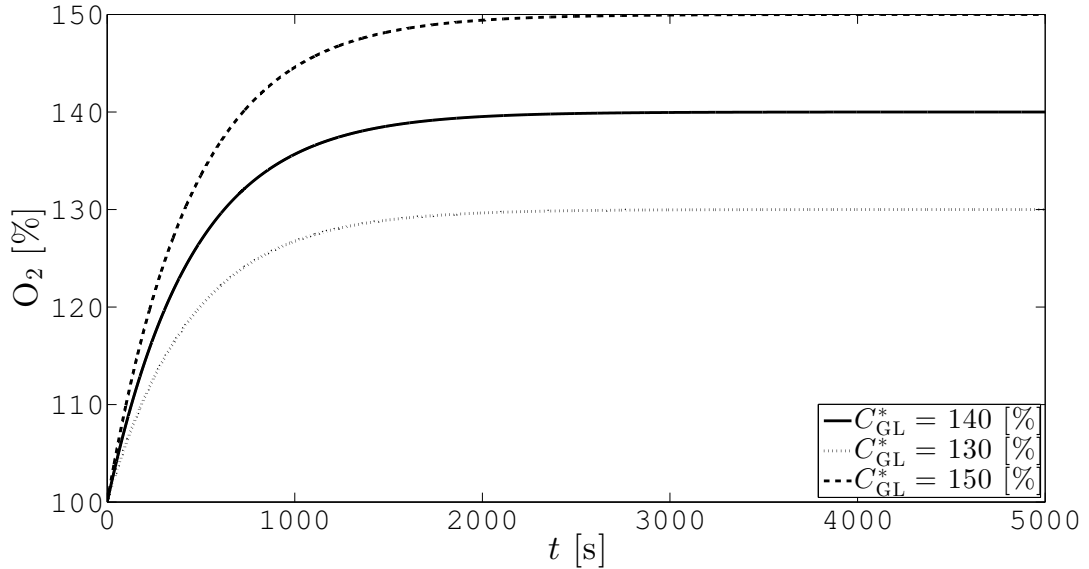


Figure 2.3: Evolution of the O_2 concentration for three different values of C_{GL}^* . $k_L a$ is the same for the three curves.

On the other hand the partial pressure of O_2 (C_{GL}^*) only influences the final or asymptotic value of $C(t)$ and the initial concentration of O_2 ($C_{0,\text{L}}$) only changes the initial value of $C(t)$. An example of the influence of C_{GL}^* can be seen on Fig. 2.3.

If the O_2 concentration in the liquid phase is known then the only unknown parameter is the $k_L a$. Manipulating Eq. 2.1 yields the following equation:

$$\ln \left(\frac{C_{GL}^* - C(t)}{C_{GL}^* - C_{0,L}} \right) = -k_L a \cdot t \quad (2.2)$$

The result of equation 2.2 are shown on Fig. 2.4. This allows to calculate the $k_L a$ through linear regression of the experimentally measured O_2 concentration as a function of time. The slope being $-k_L a$.

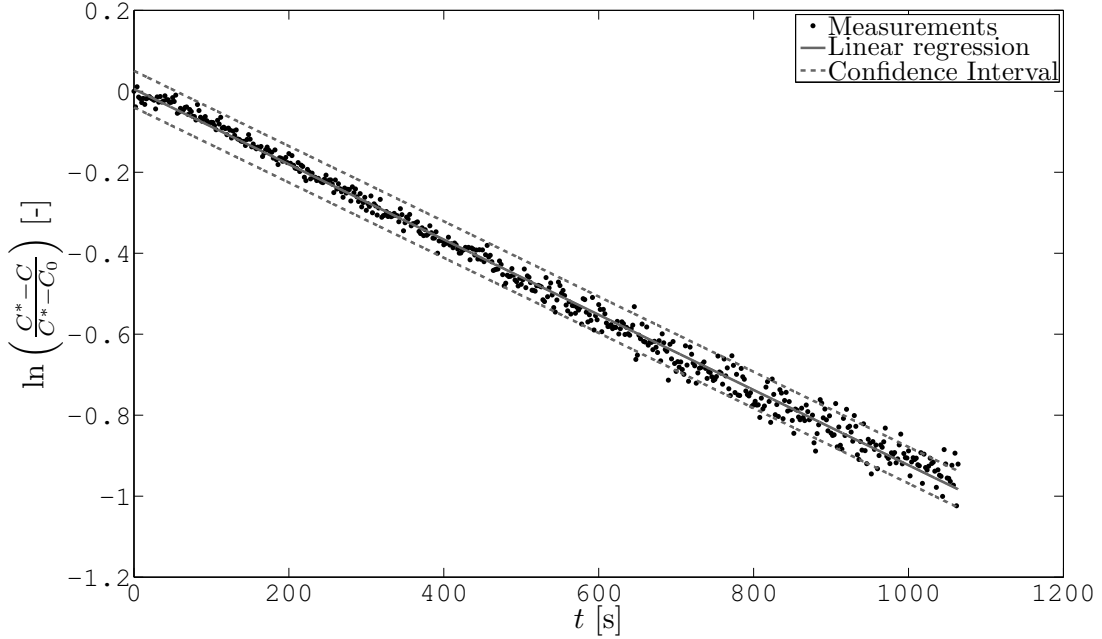


Figure 2.4: Linearization of O_2 measurements according to equation 2.2 and the corresponding linear regression and confidence interval of 95%.

2.3 Measurement routine

The experimental setup is entirely controlled by computer. The rotational speed, eccentricity and pressure are controlled by a LabVIEW[®] routine through a National Instruments[®] DAQ. This DAQ has the advantage to allow the generation and acquisition of analogical signals. This allows to build a straightforward automated measurement routine. The principle of the PSKM is to measure the evolution of O_2 in different configuration (Ω and d_s) for a given pressure $p_G = C_{GL}^*/L_{O_2}$ in the container. The only unchanged parameters are D and H_0 . The measurement has to stop when the O_2 concentration has reached $C = 0.6321C_{GL}^*$. Explanations about this choice are given later on. This routine generate the measurements files from which the $k_L a$ is then computed through a MATLAB[®] script. The steps of the routine are :

1. Reading from a batch file the amount of configuration n to be applied and setting the first duet (Ω, d_s). A waiting time of 120 seconds is observed to reach hydrodynamic stability.

2. Pressure set to p_G and begining of the acquisition of O_2 , p (the pressure inside the container), T (the temperature of the water), Ω and d_s . Acquisition stops when the condition $C = 0.6321C_{GL}^*$ is met or when the timeout is reached. $t_{out} = 3600$ s.
3. The data is saved and the pressure is set to atmospheric pressure.
4. The supersaturated water is degassed. (Ω, d_s) are set to high values (170,25) until the condition $O_2 < 100$ is met or the degassing timeout is met. $t_{out} = 1800$ s.
5. Operations 2,3 and 4 are repeated for all the duets (Ω, d_s) .

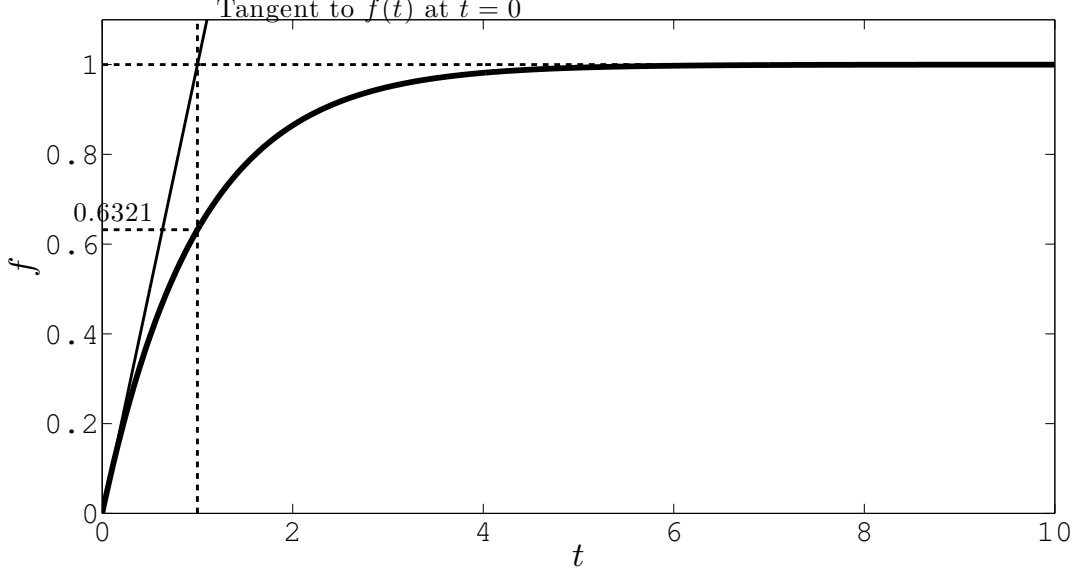


Figure 2.5: Response of a First-Order system to a step increment.

The stoping condition $C = 0.6321C_{GL}^*$ is chosen for analytical reasons. Let consider first an adimensional form of the solution of Eq. 1.5 with $k = 1$ and initial and final conditions defined as $f_0 = f(t = 0) = 0$ and $f_\infty = f(t \rightarrow \infty) = 1$ respectively. The function is then written :

$$f(t) = f_\infty - (f_\infty - f_0) \exp(-kt) = 1 - e^{-k \cdot t} \quad (2.3)$$

Graphical representation of Eq. 2.3 is shown on Fig. 2.5. If $t = 1/k$ then $f(1/k) = 1 - e^{-1} = 0.6321$. This means that $C(t)$ (Eq. 1.5) reaches 63.21% of its final value in the time corresponding to the inverse of the k_{La} . This time is called *time constant* and is often written τ . If the condition $C = 0.6321C_{GL}^*$ is not reached the k_{La} can still be computed from the slope of equation 2.2 but probably with a loss of precision.

2.4 Validation of the Measurement Technique

2.4.1 Self-validation

The accuracy of the k_{La} determination and the repeatability of the PSKM is analyzed in this section. The confidence interval of linear regression giving the k_{La} is analyzed for nine configurations : three shaking frequencies Ω/ω_{11} and for each Ω/ω_{11} three different eccentricities

\tilde{d}_s . The measurement of the $k_L a$ for those configuration is then repeated three more times to have an order of magnitude of the repeatability of the $k_L a$ measurement. Ω/ω_{11} , \tilde{d}_s and \tilde{H}_0 are chosen in the same range used on Fig. 1.5 in order to follow [12].

Ω/ω_{11} [-]	0.47			0.74			1.02		
\tilde{d}_s [-]	0.07	0.1	0.13	0.07	0.1	0.13	0.07	0.1	0.13
$k_L a$ [h^{-1}]	0.1042	0.1426	0.2598	0.9957	0.9954	3.3441	7.9296	8.7827	8.1530
ϵ_α [h^{-1}]	0.0108	0.0104	0.0111	0.0271	0.0308	0.0226	0.0228	0.0202	0.0218
ϵ_α [%]	10.3707	7.1582	4.2753	2.7141	3.0905	1.3477	0.2866	0.2297	0.2677

Table 2.1: Verification of the linear regression calculating the $k_L a$ for 3 rotational speed and 3 eccentricity. The standard deviation ϵ_α is an estimate that predicts that 95% of O_2 measurement are contained in the confidence interval (see Fig. 2.4). $\tilde{H}_0 = 0.5$

In Tab. 2.1 are found the results of the verification of OTR calculation through Eq. 2.2 whereas on Fig. 2.6 are found the results of the repetition of OTR measurement.

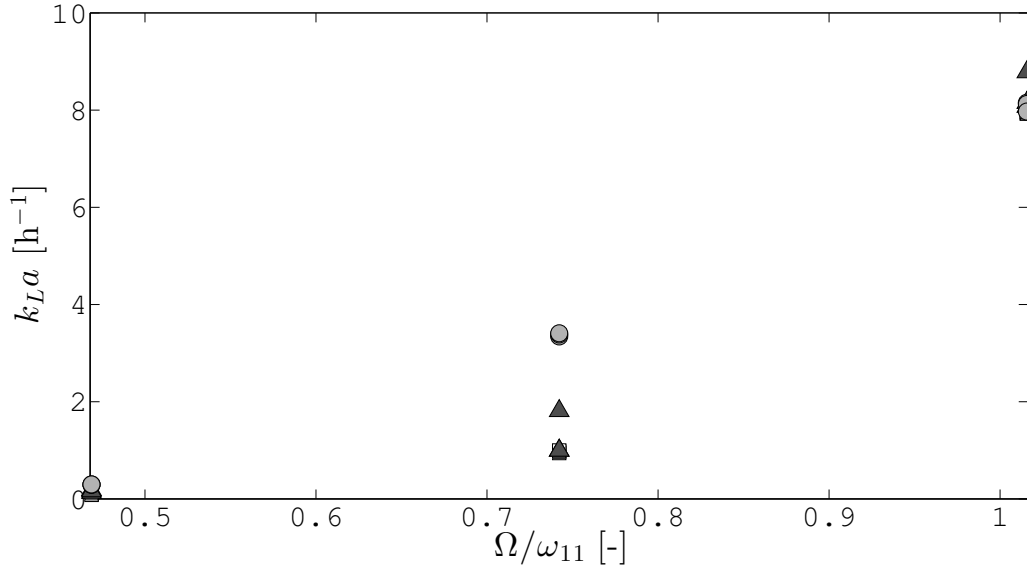


Figure 2.6: Measurements realized for the verification of the repeatability of the PSKM. The square marker correspond to $\tilde{d}_s = 0.07$, the triangular markers correspond to $\tilde{d}_s = 0.1$ and the round markers correspond to $\tilde{d}_s = 0.13$. $\tilde{H}_0 = 0.5$

On Tab. 2.1 the standard deviation ϵ_α represent the confidence interval of the linear regression where 95% of the data is found. Fig. 2.4 is an example of linear regression \bar{r} (solid grey line) and its 95% confidence interval (dashed grey line) corresponding to $\bar{r} \pm 2\epsilon_\alpha$.

It appears that the higher the $k_L a$ the lower the ϵ_α . The relative value of ϵ_α is quite high for very low $k_L a$ ($\epsilon_\alpha = 10.4\%$ for $k_L a = 0.1$). However it results in a very low maximum absolute error. Considering that a 100% confidence interval is defined as : $\bar{r} \pm 3\epsilon_\alpha$ then $3\epsilon_\alpha$ is the maximum error. Hence for $k_L a = 0.1$ the maximum error is $3\epsilon_\alpha \cong 0.03 [\text{h}^{-1}]$ which is very low in absolute terms and does not significantly affect the OTR. An example of linear regression for a low $k_L a$ is found on Fig. 2.7A. On the contrary high $k_L a$ result result in a low relative value of ϵ_α ($\epsilon_\alpha = 0.23\%$ for $k_L a = 8.78$) but a higher maximum absolute error : $3\epsilon_\alpha \cong 0.06 [\text{h}^{-1}]$. However the maximum error is still very low and has low effects on OTR. An example of linear regression for a high $k_L a$ is found on Fig. 2.7B.

Same conclusion can be drawn for the repeatability of the PSKM. From Tab. ?? it appears that the lower the $k_L a$ the higher the standard deviation ϵ but still with insignificant absolute error.

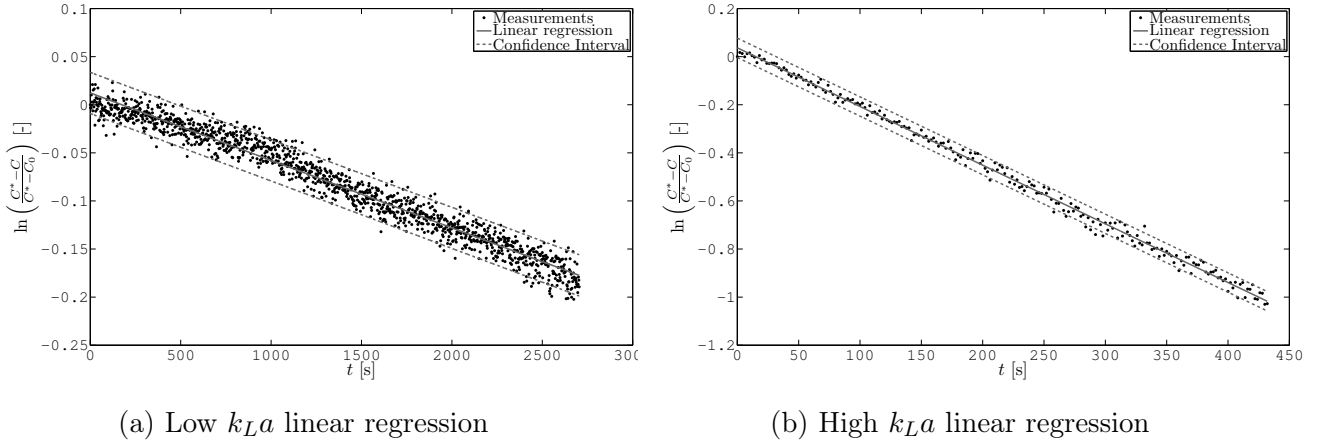


Figure 2.7: Example of two linear regression and its respective confidence interval corresponding to a low $k_L a$ and a high $k_L a$.

A special attention has to be given to the measurement realized at $\Omega/\omega_{11} = 0.74$ and $\tilde{d}_s = 0.1$. In fact this configuration corresponds to the region where the non-synchronous wave are found and where the flow pattern is strongly dependent on the followed path to reach it. On Fig. 3.9 are shown two different wave patterns corresponding to the same configuration. These particularities on the $k_L a$ will be discussed thoroughly in section 3.3.

Ultimately the PSKM technique is a reliable and repeatable OTR measurement technique.

2.4.2 Comparison of the PSKM with the gassing-out method

To test the reliability of the PSKM the results obtained by the latter are going to be compared with $k_L a$ values obtained with the gassing-out method. The value of $k_L a$ obtained from the gassing-out method are given by M. Monteil from the LBTC (Laboratoire de Biotechnologie Cellulaire). A comparison between the two measurement techniques is shown on Fig. 2.8.

From the results shown on Fig. 2.8 the following remarks can be done :

- For $\tilde{H}_0 = 0.29$ the $k_L a$ is over-estimated by the PSKM in comparison of the gassing-out method. In addition the values of the $k_L a$ for $\Omega = 90, 95, 100, 105, 125$ and 130 rpm are very different
- For $\tilde{H}_0 = 0.44$ and $\tilde{H}_0 = 0.58$ the PSKM under-estimate the $k_L a$. However the values of the $k_L a$ are quite similar mainly for $\tilde{H}_0 = 0.44$.
- The trend of all the curves (the $k_L a$ increases with Ω) is followed by the two measurement technique

It seems that the two measurement technique have quite similar results in spite of the strong discrepancy when comparing $\tilde{H}_0 = 0.29$.

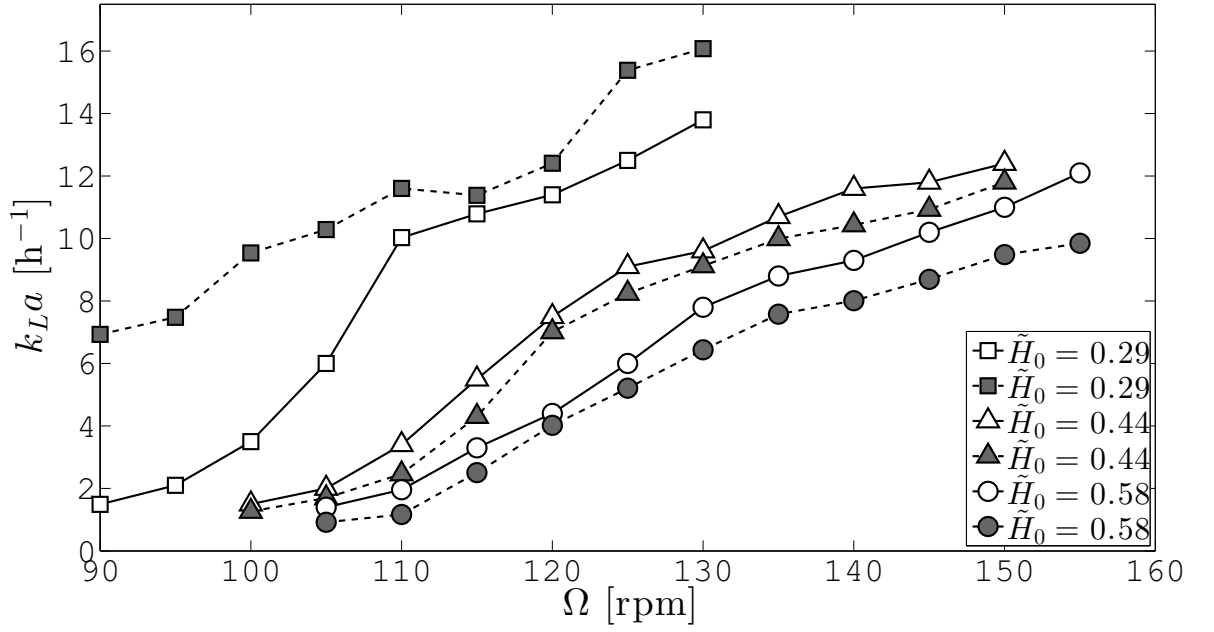


Figure 2.8: k_{La} obtained from the gassing-out method and for the PSKM method. In solid line and white marker is depicted the result for the gassing-out method whereas in dashed line and grey marker is depicted the PSKM method. Each marker correspond to a specific \tilde{H}_0 . For all the measurements $\tilde{d}_s = 0.0656$

Chapter 3

Results

3.1 Verification of the Shaking Frequency

The existence of non-synchronous wave have been discovered by Reclari [12]. However their existence is not predicted neither by the linear nor the non-linear solution of the potential model. It is then legitimate to ask whether the non-synchronous wave are intrinsic to the nature of the flow or if they are a product of external excitations. In particular small variations of the shaking frequency or the eccentricity could be the source of instabilities that ultimately result in the non-synchronous waves. It is then crucial to accurately verify the shaking frequency.

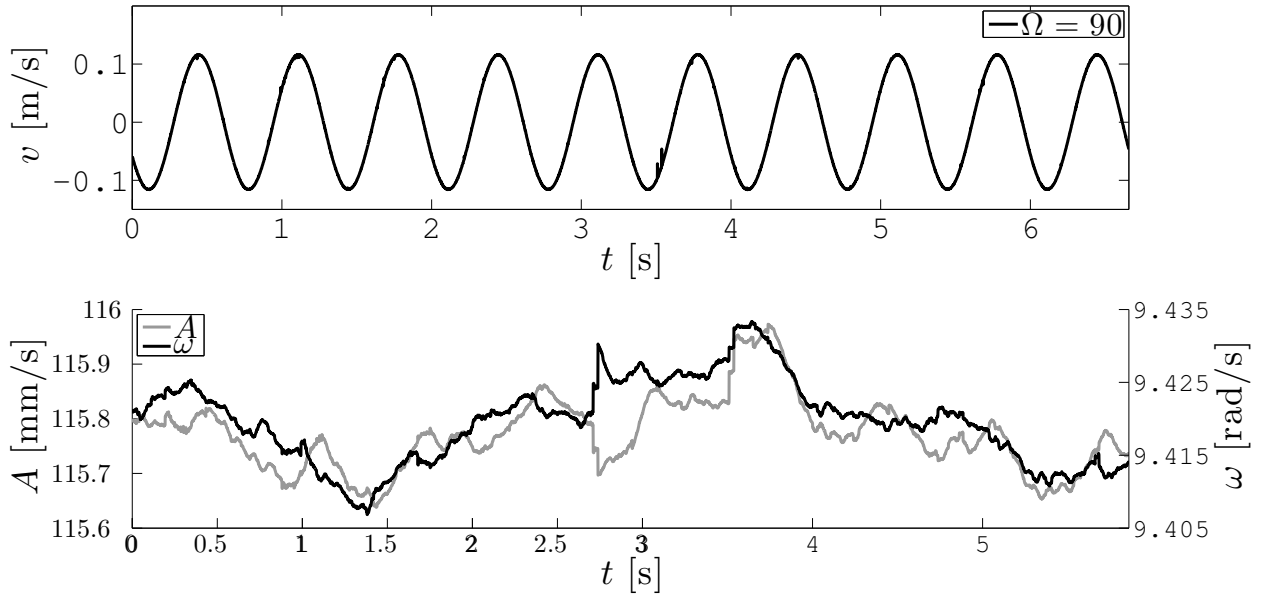


Figure 3.1: **Upper Part :** ten cycles of the monitored speed signal. **Lower Part :** Instantaneous estimation of $A(t)$ and $\omega(t)$ computed from the speed signal. $\Omega = 90$ rpm, $d_s = 25$ mm.

The speed of the shaker is monitored with a Laser Doppler Vibrometer. The laser beam is directed towards a reflective tape attached to the shaker. The relative movement of the shaker induces a doppler shift of the reflected laser beams, allowing to extract the velocity and ampli-

tude of the periodic excitations. In this case the orbital movement. The vibrometer returns an analog voltage that is acquired through the DAQ.

The orbital movement is the sum of two sinusoidal translations :

$$\vec{r} = \frac{d_s}{2} \cos(\Omega t) \vec{e}_x + \frac{d_s}{2} \sin(\Omega t) \vec{e}_y \quad (3.1)$$

The speed then reads :

$$\dot{\vec{r}} = -\frac{\Omega d_s}{2} \sin(\Omega t) \vec{e}_x + \frac{\Omega d_s}{2} \cos(\Omega t) \vec{e}_y \quad (3.2)$$

The vibrometer records the speed in one of the two direction, \vec{e}_x or \vec{e}_y . In both cases the signal is sinusoidal (see Eq. 3.2). Ten cycles of the speed signal are acquired. An example of a recorded signal is found on the upper part of Fig. 3.1.

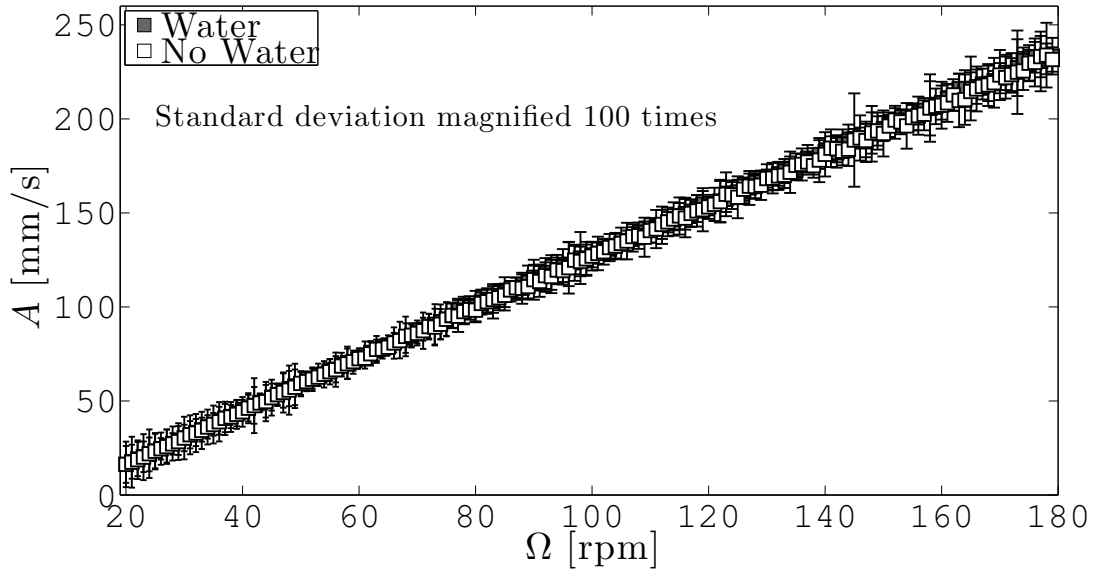


Figure 3.2: Average value of the amplitude $A(t)$ with its respective standard deviation magnified 100 times.

The signal acquired from the vibrometer is not perfectly sinusoidal. It does not exactly correspond to Eq. 3.2. Small variations in the shaking frequency or in the diameter may be sources of imprecisions. It is then more accurate to mathematically represent the signal by :

$$S(t) = A(t) \sin[\omega(t) \cdot t + \phi] \quad (3.3)$$

where $A(t)$ is the amplitude of the signal and $\omega(t)$ the shaking frequency (more precisely the shaking pulsation). Both variables are time dependant. The phase ϕ is of no interest in this particular study. It has to be noted that $A(t)$ would correspond to $\Omega d_s/2$ from Eq. 3.2 if there were no variations. An example of variation in time of A and ω is found on Fig. 3.1.

The instantaneous values of A and ω are obtained by calculating the best fitting sinusoidal curve of a portion of the signal (1.2 of a cycle). From the best fitting curve of this portion A

and ω are extracted. The Levenberg–Marquardt algorithm is used to compute the best fitting curve. The signal is swept to obtain $A(t)$ and $\omega(t)$ for the ten cycles of the signal. The step increment of the sweeping is $1/n_s$ where n_s is the sampling frequency, *i.e.* the entire signal is swept.

The average value of $A(t)$ and $\omega(t)$ are computed for a shaking frequency Ω varying from 20 rpm to 180 rpm. The measurements of the shaking frequency has been realized with and without water in the container to compare the frequency control of the shaker with and without load. The result are presented on Fig. 3.2 and Fig. 3.3 respectively. On those figure the magnitude of the standard deviation is amplified by a factor 100.

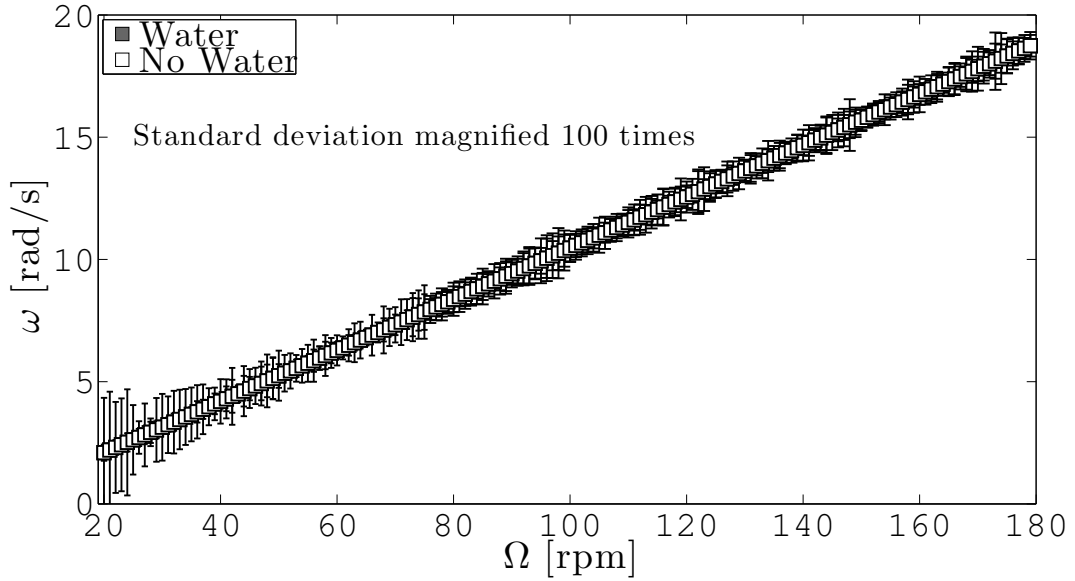


Figure 3.3: Average value of the frequency $\omega(t)$ with its respective standard deviation magnified 100 times.

The analysis of the shaking frequency reveals that there is virtually no variation in the shaking frequency that could explain the apparition of non-synchronous wave. In addition the shaker does not appear to be affected by the presence of water in the container since A and ω are the same in both case.

3.2 OTR Measurements Results

The result of the measurements realized in order to complete Fig. 1.5 with OTR data are presented in this section. To ensure coherence with [12] the same values of Ω , $\tilde{H}_0 = 0.5$ and \tilde{d}_s have been used for the measurements. The result are presented in Fig. 3.4.

From here and until the end of this Section $\tilde{\delta} = \max(\tilde{\delta}) - \min(\tilde{\delta})$ (corresponding to the measured amplitude at the wall) is going to be used for notation simplicity.

Lets consider the curve with $\tilde{d}_s = 0.07$ first (Fig. 3.5). From $\Omega/\omega_{11} = 0.4$ to 0.65 the $k_L a$ is virtually constant with some little variations. From 0.65 to 0.68 there is a little peak in the $k_L a$ that also corresponds to a peak in the $\tilde{\delta}$. Right after this peak the $k_L a$ returns to a lower value that is in the continuation of the growth tendency observed before the peak. From

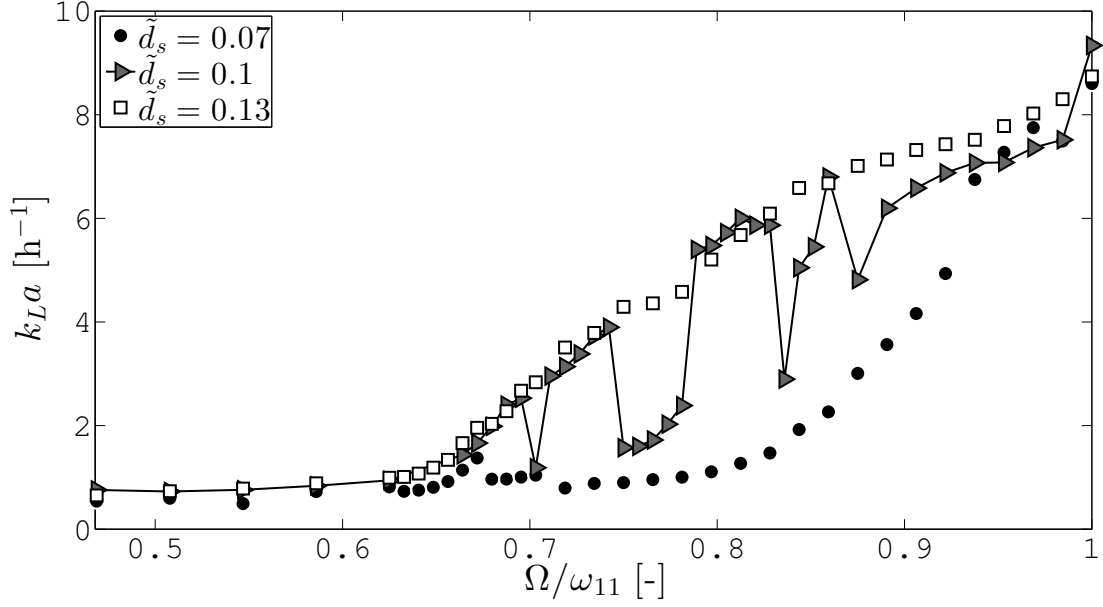


Figure 3.4: Measurement of $k_L a$ in function of the rotational speed Ω normalized by the first natural frequency ω_{11} . The values of \tilde{d}_s are $\tilde{d}_s = 0.07$, $\tilde{d}_s = 0.1$ and $\tilde{d}_s = 0.13$. The water height is $\tilde{H}_0 = 0.5$. In marker are depicted the values of the measured $k_L a$ while the solid line corresponds to the theoretical value of the water height computed with the potential solution

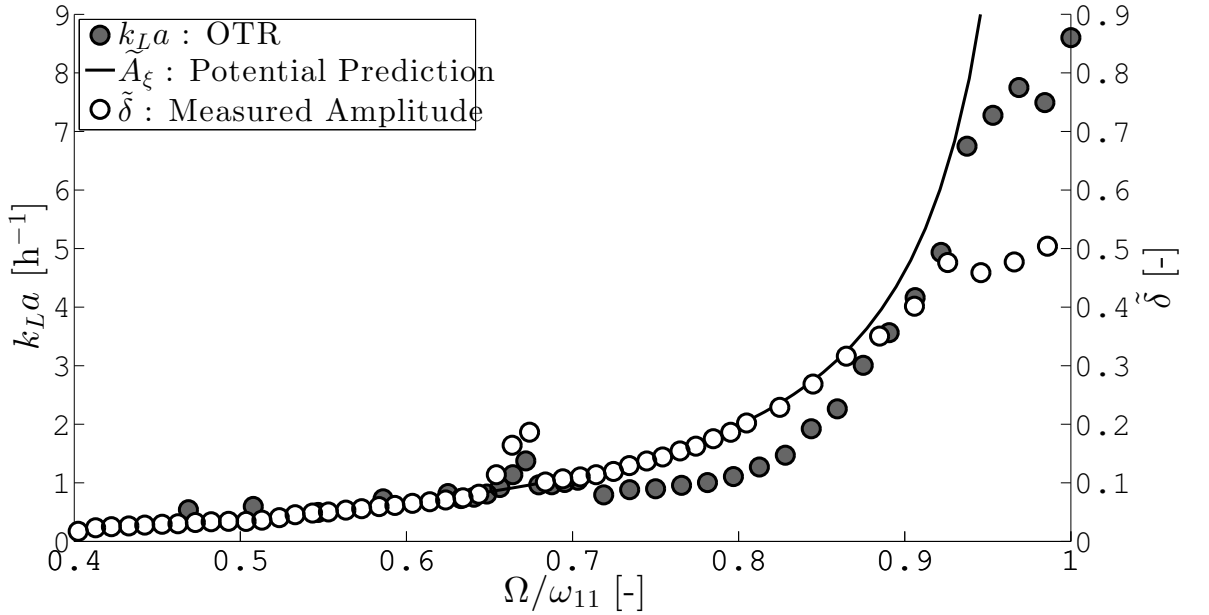


Figure 3.5: Evolution of the $k_L a$ depicted as grey round markers compared to the evolution of the measured amplitude at the container wall $\tilde{\delta}$ depicted as white round markers. In solide line is the linear potentiel prediction of the amplitude at the wall \tilde{A}_δ . $\tilde{H}_0 = 0.5$, $\tilde{d}_s = 0.07$

$\Omega/\omega_{11} = 0.68$ to 0.95 $k_L a$ experience an exponential-like growth very similar in trend to the potential prediction. On the other hand $\tilde{\delta}$ follows almost exactly the potential prediction except around $\Omega/\omega_{11} = 0.65$ and when it reaches the breaking condition (Eq. 1.4).

A similar pattern is observed for $\tilde{d}_s = 0.13$ (Fig. 3.6). From $\Omega/\omega_{11} = 0.4$ to 0.6 the growth rate

of both $k_L a$ and $\tilde{\delta}$ is virtually constant but in general higher in value than for $\tilde{d}_s = 0.07$ and $\tilde{d}_s = 0.1$. This should come as no surprise since from the potential solution of the amplitude (Eq.1.2) the height of the wave is directly proportional to the eccentricity. When Ω/ω_{11} reaches approximately 0.65 the values of the $k_L a$ and $\tilde{\delta}$ start to grow at a very high rate (same order of magnitude as for $\tilde{d}_s = 0.07$). However in this case the difference is that both $k_L a$ and $\tilde{\delta}$ are not subject to a peak around $\Omega/\omega_{11} = 0.65$ (as on Fig. 3.5), their growth rate is maintained much longer. When $\Omega/\omega_{11} = 0.7$ approximately the growth rate of $\tilde{\delta}$ decreases. The wave height reaches the breaking condition. This deceleration of the growth rate is also observed in the $k_L a$ but it occurs later, around $\Omega/\omega_{11} = 0.85$ and is less pronounced.

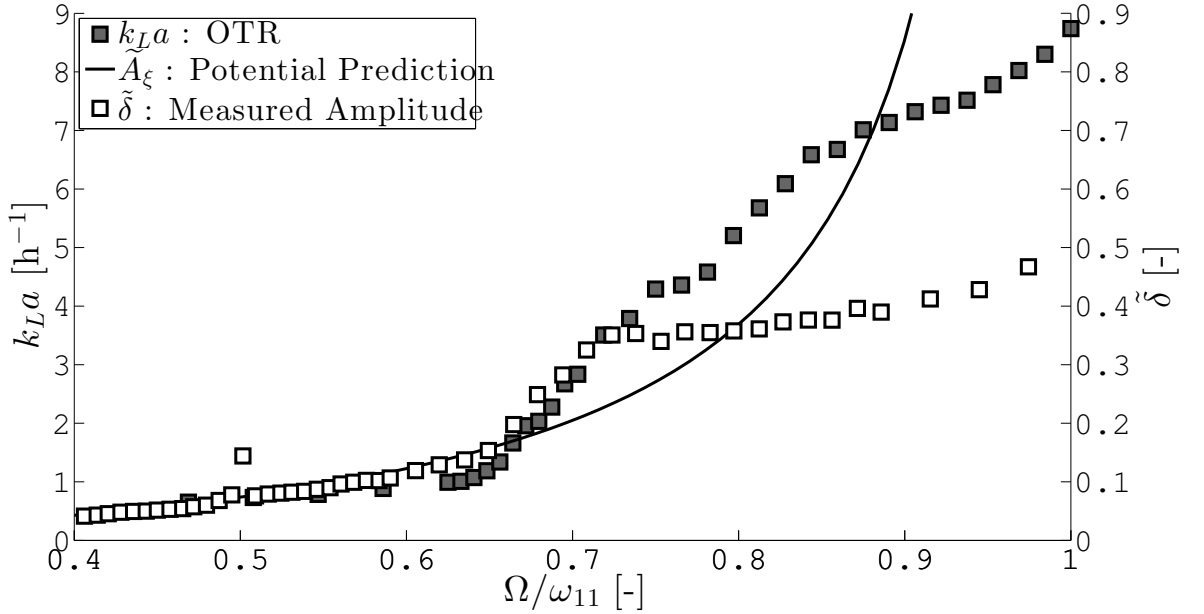


Figure 3.6: Evolution of the $k_L a$ depicted as grey square markers compared to the evolution of the measured amplitude at the container wall $\tilde{\delta}$ depicted as white square markers. In solid line is the linear potential prediction of the amplitude at the wall \tilde{A}_δ . $\tilde{H}_0 = 0.5$, $\tilde{d}_s = 0.13$

As can be seen on Fig. 3.4 the values of $k_L a$ for $\tilde{d}_s = 0.1$ seem to follow the same pattern as for $\tilde{d}_s = 0.13$ but have serious discontinuities. They will be discussed deeply on Section 3.3.

The explanation of the accelerated growth that occurs around $\Omega/\omega_{11} = 0.65$ is found through the existence of natural sub-harmonics of natural modes. It happens that $\Omega/\omega_{11} = 0.65$ corresponds to the sub-harmonic $\omega_{21}/2$ and it is the origin of the peak of amplitude around this frequency. The other sub-harmonic observed on Fig. 1.5 are $\Omega/\omega_{11} = 0.5$ and $\Omega/\omega_{11} = 0.33$ which correspond to the sub-harmonics $\omega_{11}/2$ and $\omega_{11}/3$ ($p = 2, 3$ respectively). It is interesting to observe that the sub-harmonics "enhance" the $k_L a$ in a similar fashion that they accentuate the wave amplitude

A general conclusion that can be drawn from Fig. 3.4 is that the OTR seems to be strongly linked to the hydrodynamics of the flow. This should not come as a big surprise since Oxygen Transfer occurs at the boundary Gas-Liquid and as all transport phenomenon it is intrinsically linked to the state of the boundary layer. On the other hand the remarkable similarities between the trend in the $k_L a$ and the $\tilde{\delta}$ suggest that there may be a proportionality link between the two, *i.e.* it may be possible to express an order of magnitude of the $k_L a$ from the knowledge of $\tilde{\delta}$ only.

3.3 Non-synchronous wave pattern and OTR measurements

A particular wave pattern has been shown to exist, the non-synchronous wave [12]. This wave pattern is particular in the sense that it does not respect the frequency of agitation. In other words one cannot find a reference frame rotating around the revolution axis of the vessel which will make the wave appear motionless. It appears for $\tilde{d}_s \cong 0.1$ just before breaking inception, hence $\Omega/\omega_{11} = 0.65$ to 0.9 .

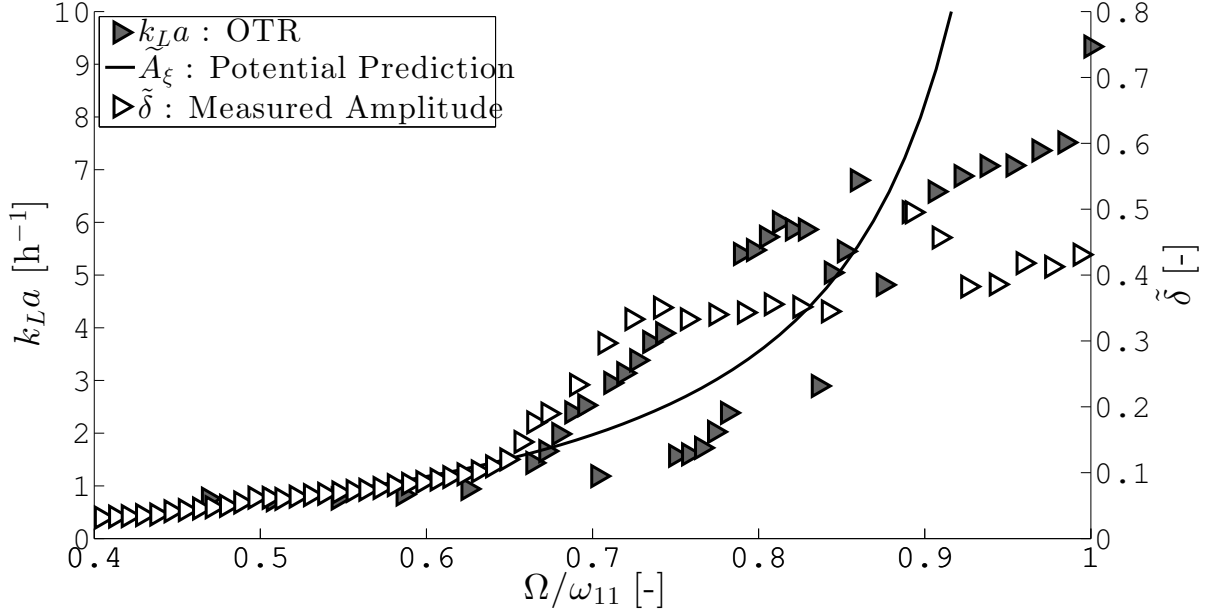


Figure 3.7: Evolution of the $k_L a$ depicted as grey triangular markers compared to the evolution of the measured amplitude at the container wall $\tilde{\delta}$ depicted as white triangular markers. In solid line is the linear potential prediction of the amplitude at the wall \tilde{A}_δ . $\tilde{H}_0 = 0.5$, $\tilde{d}_s = 0.1$

Having that in mind, it is now possible to analyse more in detail the results of the $k_L a$ from Fig. 3.4 for $\tilde{d}_s = 0.1$. Fig. 3.8 is a zoom of Fig. 3.4 and 3.7 for $\Omega/\omega_{11} = 0.7$ to 0.86 .

From this figure several conclusions come to mind:

- For some rotational speed the measurements are very close one from the other and the error is more likely to come from some uncertainty in the measurement
- For other rotational speed such as $\Omega/\omega_{11} = 0.7$, $\Omega/\omega_{11} = 0.74$ or $\Omega/\omega_{11} = 0.8$ to 0.84 such a dispersion of the measurement cannot be explained by some uncertainty

It has to be remarked that for a given configuration (a set of Ω/ω_{11} , \tilde{H}_0 and \tilde{d}_s) two flow regimes are observed something which is not predicted by the potential flow (see Fig. 3.9). In this particular situation where $\tilde{d}_s = 0.1$ and $\Omega/\omega_{11} > 0.65$ the flow is just in the boundary of breaking/non-breaking so it cannot be considered as purely potential. This leads to a strong hysteresis phenomena : depending on the chosen path to reach a particular regime, the wave can be synchronous or non-synchronous. Two path to reach the synchronous or non-synchronous wave pattern have been identified :

- **Upward approach :** the speed is increased progressively (step increment of 5 or 10 rpm) to reach a desired speed, say $\Omega/\omega_{11} = 0.81$ (Fig. 3.9A).

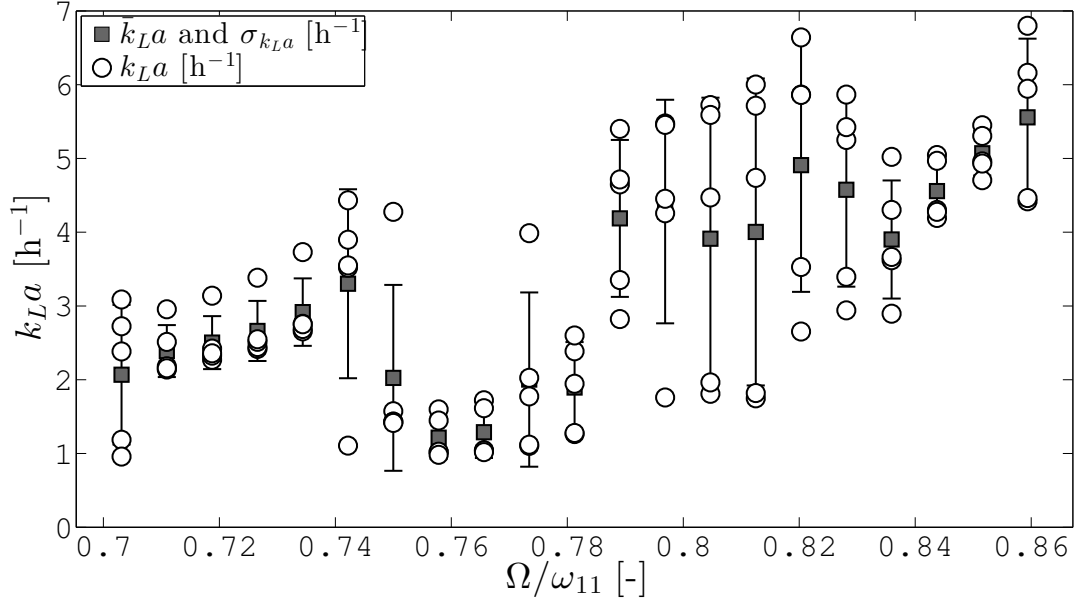


Figure 3.8: Measurements of the k_La for a non-synchronous wave. The average and standard deviation are realized over 5 measurements. $\tilde{d}_s = 0.1$ and $\tilde{H}_0 = 0.5$

- **Downward approach** : the starting speed is set high (by high is intended beyond $\Omega/\omega_{11} = 1$ when the breaking has already occurred, say $\Omega/\omega_{11} = 1.2$) and then it is decreased, progressively or not to reach a desired speed, say $\Omega/\omega_{11} = 0.81$ (Fig. 3.9B)



(a) Downward approach



(b) Upward approach

Figure 3.9: Two wave patterns corresponding to the same configuration : $\tilde{H}_0 = 0.5$, $\Omega/\omega_{11} = 0.81$, $\tilde{d}_s = 0.1$

It appears that the flow regime resulting from the Downward Approach possesses a higher k_La . As an example for $\Omega/\omega_{11} = 0.81$, $k_La = 5.5$ results from the Downward Approach whereas $k_La = 1.8$ results from the Upward Approach (Fig. 3.8). In addition the wave pattern can also be non-synchronous. As an example for $\Omega/\omega_{11} = 0.71$ the lowest values of OTR ($k_La = 1$) were measured for non-synchronous waves pattern. It appeared with the Upward Approach. Downward Approach resulted in higher k_La but not necessarily a non-synchronous flow regime. However it has not been clear if the difference in OTR is due to the non-synchronicity or to the followed path in this particular case.

Due to the particular behavior of the OTR for $\tilde{d}_s = 0.1$ and $\Omega/\omega_{11} > 0.65$, let this eccentric-

ity diameter be called *Critical Diameter* and written \tilde{d}_s^* . Similarly let the region going from $\Omega/\omega_{11} = 0.65$ to $\Omega/\omega_{11} = 0.9$ (the breaking) be called *Critical Region*.

3.4 Discussion about the results obtained

3.4.1 Measurement Technique

There are two general conclusions that can be drawn from the verification of the measurement technique. The first one is that the PSKM seems to be a very robust method since there is little uncertainty in the calculation of the $k_L a$ as illustrated in Tab. 2.1 and in the repetition of the measurement. The second conclusion is that in spite of the fact that their results are quite alike, the PSKM and gassing-out method do not give the exact same results but seem to follow this general trend:

- For lower \tilde{H}_0 the PSKM overestimate the $k_L a$, or reciprocally the gassing-out underestimate the $k_L a$
- For higher \tilde{H}_0 the PSKM underestimate the $k_L a$, or reciprocally the gassing-out overestimate the $k_L a$

No information have been found in the litterature, however it may be possible to have an insight of the difference between the two method considering the following : the gassing-out method involves two gases (O_2 and generally N_2 to purge O_2) whereas the dynamics method only involve one. At the boundary when the supply of N_2 toggles towards O_2 the mixture of both gas in the liquid phase may provoke errors in the O_2 monitoring hence in the determination of the $k_L a$.

3.4.2 Influence of the specific area on the OTR

As mentioned in Chapter 1 the $k_L a$ is proportional to the specific area a which is the ratio between the gas-liquid interface area over the liquid volume. If one consider as a simplistic approximation the wave pattern as a cylindrical segment, it is then pretty natural to predict the increase of $k_L a$ with an increasing wave heighth. A cylindrical segment is defined as the intersection of a circular cylinder with two or more planes. In particular if one of the two planes is normal to the axis of the cylinder and the other one is inclined with an angle α with respect to it the geometrical figure obtained and the wave pattern are quite alike (see Fig. 3.9B). A representation of a cylindrical segment is shown on Fig. 3.10.

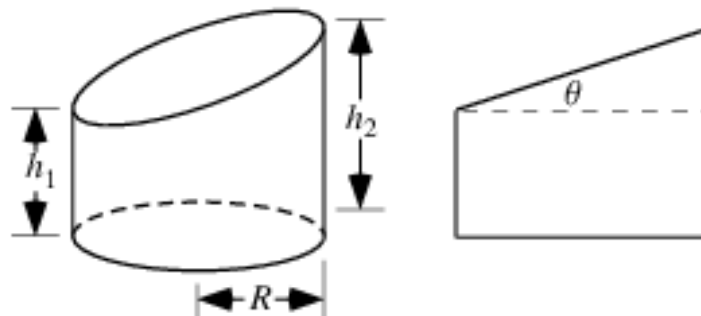


Figure 3.10: Geometrical properties of a cylindrical segment. [6]

Its geometrical properties are :

- $r = D/2$, the dimensionless form is then $\tilde{r} = 1/2$
- $h_1 = H_0 - \delta/2$, the dimensionless form is then $\tilde{h}_1 = \tilde{H}_0 - \tilde{\delta}_s/2$
- $h_2 = H_0 + \delta/2$, the dimensionless form is then $\tilde{h}_2 = \tilde{H}_0 + \tilde{\delta}_s/2$
- $\tan \theta = (h_2 - h_1)/2 = \tilde{h}_2 - \tilde{h}_1$

The area of the intersection between the plane and the cylinder is an ellipse. Its area is written : $a = \pi ab$ where $a = r$ is the semiminor axis and $b = \frac{1}{2}\sqrt{(2r)^2 + (h_2 - h_1)^2}$ the semimajor axis [6]. Knowing the volume $V = \pi r^2 H_0$, the specific surface area may then be written:

$$a = \frac{\sqrt{1 + \tilde{\delta}^2}}{2H_0} \quad (3.4)$$

A graphical representation of a and $k_L a$ in function of $\tilde{\delta}$ is found on Fig. 3.11.

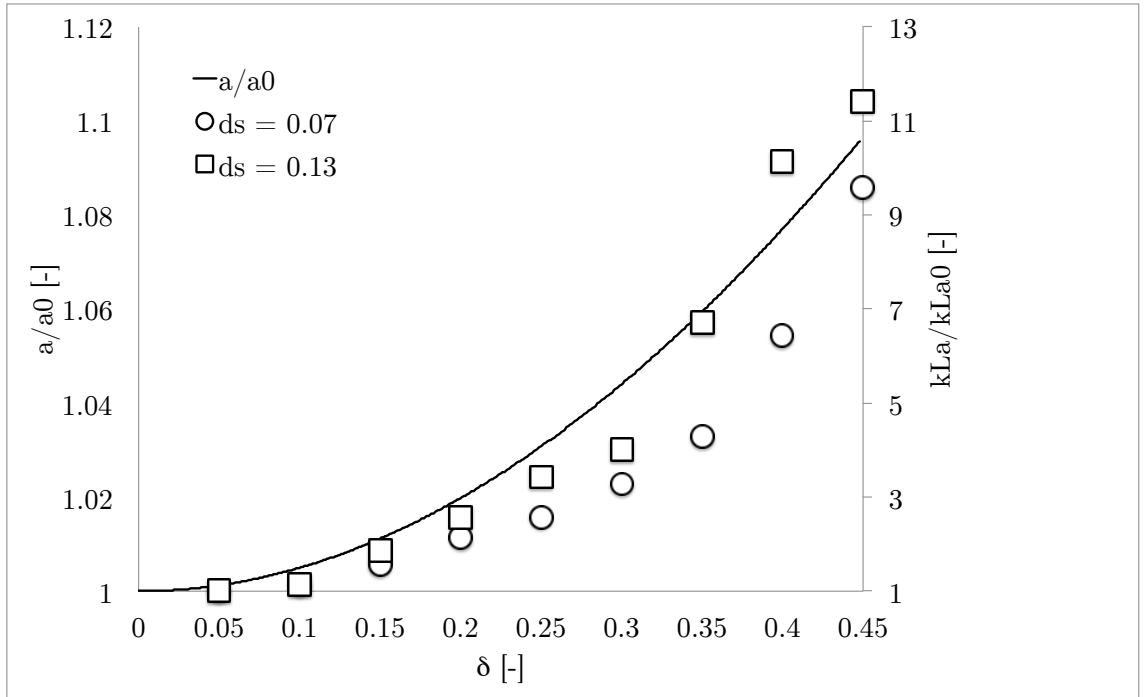


Figure 3.11: Evolution of the ratio a/a_0 and $k_L a$ in function of the wave amplitude $\tilde{\delta}_s$, a_0 being the initial value.

It clearly appears that the evolution of a cannot explain alone the evolution of the $k_L a$. From Fig. 3.11 we can see that the $k_L a$ goes from 0.7 to 9 h^{-1} which correspond to an increment of $> \times 15$ approximately (for $\tilde{d}_s = 0.07$ and 0.13). On the other hand the increment of a is barely of $\times 1.1$ according to the cylindrical segment approximation. Even if this approximation is quite coarse, the real surface increment due to the wave height increment can hardly be more than $\times 3$ the cylindrical segment approximation. It is still not enough to account for the $k_L a$ increment. A similar result has been achieved by [17], the conclusion of the study was that $k_L a$ increment was more due to turbulence in the boundary layer due to micro-breaking which in terms causes an increment in k_L more than a . A similar conclusion can be drawn here.

3.4.3 Summary

One can more or less intuitively associate movement of water, and in particular its free surface with an enhanced gas exchange or enhanced exchange in general between the liquid and the gas. This is in perfect correlation with the results obtained in this Chapter :

- The greater the agitation speed, hence the faster the movement the greater the k_La
- The greater the eccentricity, hence the wider the movement the greater the k_La

However some results obtained where not expected and are not intuitive and may be undesirable for cellular culture. The different regimes that the flow undergoes when $\tilde{d}_s \cong 1$ and the very different values of the k_La that can be obtained from a single configuration were not expected. In particular the fact that the followed path to reach a desired configuration bear great importance on the flow regime (hence on its respective OTR) has not been studied by Reclari [12]. The non-synchronous wave also seem to have a negative influence on the k_La . However it has not been possible to clearly identify its effect since its appearance is linked to the followed path. As mentionned in Section 3.4.2 the area increase from $\tilde{\delta}_s = 0$ to 0.443 is not enough to explain the changes in the k_La , it will certainly not be able to explain the changes in the k_La for a single configuration. The explanation has to be found in the increase of turbulence in the air-water interface [8] [11] [9] [17]. However since turbulence has not been the purpose of the study its effects are barely mentioned but not detailed.

Chapter 4

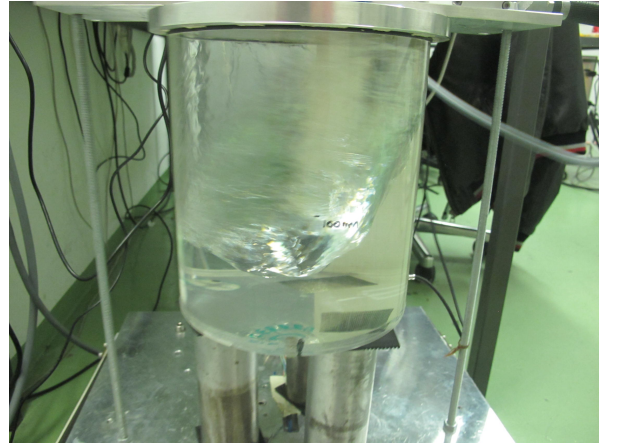
Peculiar Waves

4.1 Description

In the course of the experiments, a peculiar behavior of the wave that occurs beyond the first natural mode (1,1) and which deserves deeper investigations in the future have been accidentally discovered. For particular operating conditions, it has been observed that the wave pattern may be deeply different depending on how the rotation speed is reached. This phenomenon is illustrated on Fig. 4.1. A high amplitude wave is obtained by gradually increasing the the shaking frequency as usually done in [12], Fig. 4.1B. The peculiar wave with much lower amplitude obtained for the same operating condition with fast increase of the shaking frequency, Fig. 4.1A.



(a) Peculiar wave



(b) Non peculiar wave

Figure 4.1: Comparison between the peculiar wave and the non peculiar. $\tilde{H}_0 = 0.5$, $\tilde{d}_s = 0.042$, $\Omega/\omega_{11} = 1.75$

The peculiar wave is attained only for low eccentricities, namely $\tilde{d}_s < 0.063$. If \tilde{d}_s is low enough and the shaking frequency is reached quickly then the wave pattern will be peculiar. If however \tilde{d}_s is low enough but the shaking frequency is reached gradually the non peculiar wave pattern is reached (see Fig. 4.1B). There is also a limiting frequency, *i.e.* if the final speed is reached quickly but it is not high enough then the peculiar wave will not be attained. However a lower speed limit has not been clearly identified. A general rule of thumb is to set the target speed

above $\Omega/\omega_{11} = 1.56$. Another interesting property of the peculiar wave is its strong persistence. Once the regime is set, it is possible to change the operating parameters (Ω and d_s) in a wide range and still be in the peculiar regime. As a matter of fact it is possible to higher than $\tilde{d}_s = 0.063$ and below $\Omega/\omega_{11} = 1.56$.

It is interesting to note that a similar situation has been reported in [12]. For extremely low diameter ($\tilde{d}_s = 0.01$) the wave pattern recovers from the breaking and return to the predicted potential solution (see Fig. 4.2). In the case of peculiar wave, the system behave as if the quick passage through the first natural mode (1,1) allows the flow to skip or recover from the breaking.

On Fig. 1.4 the natural modes predicted by the potential solution are shown, black and white region corresponding to vertical extremums while grey regions remains at $z = 0$ (the height of water when the shaker is at rest). Comparing Fig. 4.1A with the theoretical mode corresponding to ω_{12} on Fig. 1.4 one can suppose that this Peculiar Wave corresponds to the natural mode $m = 1, n = 2$. In fact on Fig. 4.1A the maximum and minimum amplitudes are found near the center of the liquid bulk, which is what is depicted on Fig. 1.4. It has to be noted however that for $\tilde{H}_0 = 0.5$, $\omega_{12} = 23.4631$ Hz which corresponds to 224 rpm, it means that amplitude should tend towards infinite values which is not the case here.

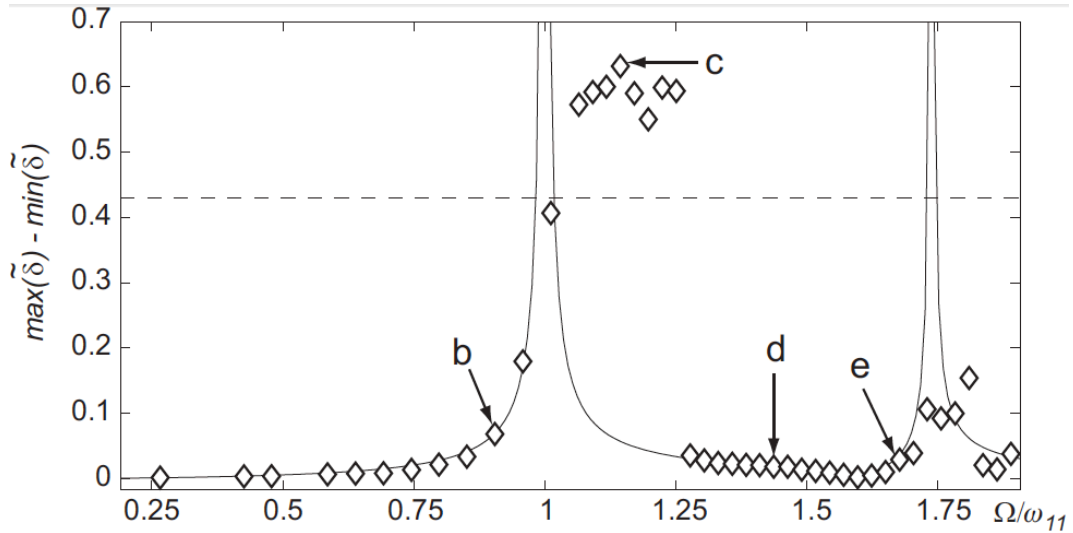


Figure 4.2: Evolution of the free surface amplitude of the wave for $\tilde{H}_0 = 0.5$, $\tilde{d}_s = 0.01$ and varying Ω/ω_{11} (from [12]).

4.2 OTR Measurements

No information about the hysteresis wave have been reported in [12] and in the litterature. It seemed interesting to try to charecterize some of its features. The first step followed in this study is to compare its OTR with the OTR of the normally expected wave (by abuse of langage let this wave pattern be denominated normal wave in constrast to peculiar wave). The results are found on Fig. 4.3.

It clearly appears that OTR is very different according to the wave pattern, the Peculiar Wave have a much lower $k_L a$. This result is in agreement with the general tendency observed in Chap. 3 since its wave amplitude is pretty low (see Fig. 4.1A). However it is interesting to

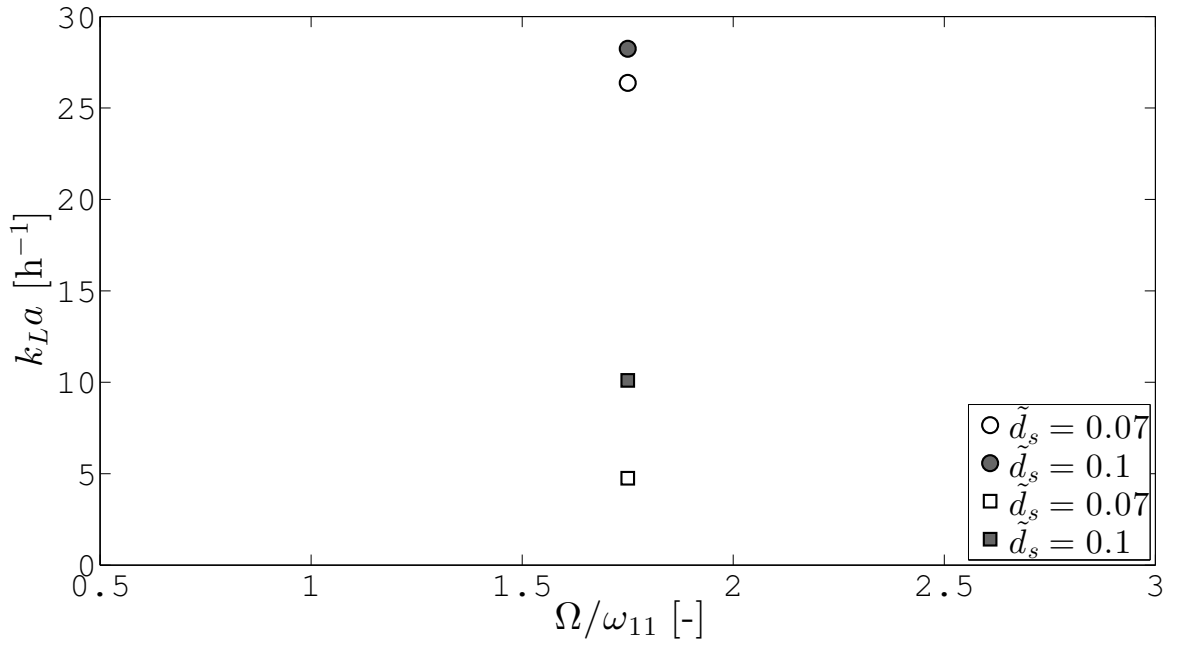


Figure 4.3: Measurement of the $k_L a$ for hysteresis waves depicted by square markers pattern compared to the normal wave pattern obtained with the same configuration, depicted by round markers. $\tilde{H}_0 = 0.5$

note that for a little \tilde{d}_s increment (0.03) the $k_L a$ is virtually doubled, whereas for the normal wave for the same \tilde{d}_s increment is about the same order of magnitude as the $k_L a$.

Conclusion

In the present study an experimental investigation of the flow field and Oxygen Transfer Rate (OTR) in Orbital Shaken Bioreactor has been performed. To this end, the experimental setup developed by M. Reclari [12] has been used and a measurement technique for the $k_L a$ determination, based on the so-called Pressure Step Increment method has been implemented. This method belongs to the family of Dynamic Pressure Method techniques. A special device was designed to allow for pressure variations within the container while the oxygen content in the liquid phase was monitored with the help of an optical oxygen probe located at the bottom the container. A high speed camera was used to visualize the wave shape. The operating conditions were varied in a wide range and the main results may be summarized as follows :

- The Pressure Step Increment method has proven to be efficient and accurate for the evaluation of the $k_L a$. Unlike the widely used Gassing-out method, there is no need for additional gas (N_2) and the measurement duration is reduced.
- It was found that the OTR is intimately linked to the wave amplitude, as far as the eccentricity is above or below the Critical Diameter $\tilde{d}_s^* = 0.1$. In this case increasing the wave amplitude result in increasing the OTR. For the particular case when $\tilde{d}_s^* = 0.1$, it is as if the strong changes in oxygenation performances are due to the fact that the wave becomes unstable switching back and forth from single to double crested wave in a non-predictable way. As a result, the OTR may vary significantly for a small variation of the shaking speed. Further investigations should be carried out to better understand and master this type of waves.
- It has been demonstrated that the non-synchronous waves are an intrinsic property and are not due to external excitations. In fact the follow-up of the shaking speed did not reveal any significant parasitic acceleration that might trigger a non-synchronous behavior. In addition it has been shown that non-synchronous waves are hardly reproducible and are strongly dependent on the path used to reach them. Nevertheless in isolated cases it has been observed that non-synchronous waves exhibit lower OTR compared to synchronous breaking waves obtained for the same operating conditions but different followed path.
- A peculiar behavior of the wave that occurs beyond the first resonance mode at low excentricity has been discovered accidentally. Depending on whether the shaking frequency is reached gradually or rapidly, the wave may exhibit respectively large amplitude and high OTR or much lower amplitude and lower OTR.

Bibliography

- [1] BANNER, M. L., AND PHILLIPS, O. M. On the incipient breaking of small scale waves. *Journal of Fluid Mechanics* 65 (1974), 647–656.
- [2] CSANADY, G. T. The role of breaking wavelets in air-sea gas transfer. *Journal of Geophysical Research* 95 (1990), 749–759.
- [3] GARCIA-OCHOA, F., AND GOMEZ, E. Theoretical prediction of gas-liquid mass transfer coefficient, specific area and hold-up in sparged stirred tanks. *Chemical Engineering Science* 59 (2004), 2489–2501.
- [4] GARCIA-OCHOA, F., AND GOMEZ, E. Bioreactor scale-up and oxygen transfer rate in microbial processes: An overview. *Biotechnology Advances* 27 (2009), 153–176.
- [5] GAUTHIER, L., THIBAUT, J., AND LEDUY, A. Measuring kla with randomly pulsed dynamic method. *Biotechnology and Bioengineering* 37 (1991), 889–893.
- [6] HARRIS, J. W., AND STÖCKER, H. *Handbook of Mathematics and Computational Science*. Springer, 1998.
- [7] HIGBIE, R. The rate of absorbtion of a pure gas into a still liquid during short periods of exposure. *Institution of Chemical Engineers* 35 (1935), 36–60.
- [8] JÄHNE, B., AND HAUSSECKER, H. Air-water gas exchange. *Annual Reviews of Fluid Mechanics* 30 (1998), 443–468.
- [9] JÄHNE, B., MÜNNICH, O. K., BÖSINGER, R., DUTZI, A., HUBER, W., AND LIBNER, P. On the parameters influencing air-water gas exchange. *Journal of Geophysical Research* 92 (1987), 1937–1949.
- [10] MAIER, U., LOSEN, M., AND BÜCHS, J. Advances in understanding and modeling the gas-liquid mass transfer in shake flasks. *Biochemical Engineering Journal* 17 (2004), 155–167.
- [11] MELVILLE, W. K. The role of surface-wave breaking in air-sea interaction. *Annual Reviews of Fluid Mechanics* 28 (1996), 279–321.
- [12] RECLARI, M. *Hydrodynamics of Orbital Shaken Bioreactor*. PhD thesis, EPFL - Lausanne, 2013.
- [13] STETTLER, M. *Bioreactor processes based on disposable materials for the production of recombiant proteins from mammalian cells*. PhD thesis, EPFL - Lausanne, 2007.
- [14] SURESH, S., SRIVASTAVA, V., AND MISHRA, I. Techniques for oxygen transfer measurement in bioreactors: a review. *Wiley Interscience* (March 2009).

- [15] VANDERKOOI, J. M., MANIARA, G., GREEN, T. J., AND WILSON, D. F. An optical method for measurement of dioxygen concentration based upon quenching of phosphoresce. *The Journal of Biological Chemistry* 262 (1987), 5476–5482.
- [16] VARDAR, F., AND LILLY, M. D. The measurement of oxygen-transfer coefficients in fermentors by frequency response techniques. *Biotechnology and Bioengineering* 24 (1982), 1711–1719.
- [17] WURM, F. M., BÜRKI, C.-A., DEJESUS, M., DE SANCTIS, D., DISCACCIATI, M., HACKER, D. L., PAROLINI, N., PERRONE, M., QUARTERONI, A., AND ZHANG, X. Efficient oxygen transfer by surface aeration in shaken cylindrical containers for mammalian cell cultivation at volumetric scales up to 1000 l. *Biochemical Engineering Journal* 45 (2009), 41–47.
- [18] ZAPPA, C. J., ASHER, W. E., AND JESSUP, A. T. Microscale wave breaking and air-water gas transfer. *Journal of Geophysical Research* 106 (2001), 9385–9391.